History and Dynamics of Explosive Volcanism at Tseax Cone, British Columbia

by

Rose Gallo

A THESIS SUBMITTED IN PARTIAL FULFILLMENT OF THE REQUIREMENTS FOR THE DEGREE OF

BACHELOR OF SCIENCE (HONOURS)

in

THE FACULTY OF SCIENCE

(Geological Sciences)

This thesis conforms to the required standard of

…….

Supervisor

THE UNIVERSITY OF BRITISH COLUMBIA

(Vancouver)

April 2018

ABSTRACT

The eruption of Tseax Cone, approximately 320 years ago, is thought to be the deadliest volcanic eruption in Canadian history, resulting in the deaths of an estimated 2000 people. This small eruptive center in northern British Columbia comprises two cinder cones, a highly dissected spatter cone, a tephra deposit covering an approximate area of 2.2×10^7 m^2, and a 32 km long lava flow. New geochemical, paleomagnetic, petrographic and field data are drawn upon to propose a new hypothesis that all eruptive materials at Tseax were produced during a single period of activity. The eruptive sequence is shown to begin with low energy fire fountaining forming a small cinder cone approximately 60 m in diameter and a spatter cone 460 m in diameter. Higher energy fountaining activity from a new vent, slightly offset within the spatter cone, and the production of a tephra column slightly more than 5 km high and lasting for approximately one day followed the first eruptive phase. The high energy phase produced a larger cinder cone and a highly asymmetric, northeast elongate, tephra deposit. The final phase of the eruption was the extrusion of the lava flow accompanied by a final sputtering of ballistics from the main vent.

TABLE OF CONTENTS

ACKNOWLEGEMENTS

I would like to thank Yannick le Moigne, to whose PhD research my work will hopefully contribute, for his assistance in the field and his guidance and contribution of data throughout the development of this thesis. I would also like to thank his field assistant Rachel Warwick for her assistance in the collection of my field data and for her positive attitude even when covered in bear spray.

I am thankful for the guidance of the graduate students of the UBC Volcanology and Petrology Lab; Amy Ryan, Alex Wilson, Ryan Kroner and David Sasse. I would especially like to thank Amy for instructing me in the use of the Mastersizer, pycnometer, rock saw, rock drill, and other lab equipment. I would like to thank Alex for his guidance in dealing with GIS problems and teaching by example how to retain sight of the big picture.

Most importantly I would like to thank my supervisor Dr. Kelly Russell, for encouraging me to ask more and better questions and insisting that I commit to an interpretation of my data. I appreciate his constant willingness to discuss my questions and challenges no matter how strange.

1. INTRODUCTION

Tseax Cone, also known as Aiyansh Volcano, is a small monogenetic eruptive center located within Nisga'a Provincial Park in northwestern B.C. The volcano consists of a central 290 m wide cinder cone set within a slightly offset and highly dissected, oxidized outer spatter cone measuring 460 m in diameter (Wuorinen 1978). A smaller approximately 60 m wide cinder cone, referred to here as the parasitic cone, is situated 240 m north of the main cone. It consists of highly oxidized lapilli, has an asymmetrical crater which tilts to the northeast and is associated with a series of small cinder mounds which may have formed a linear vent.

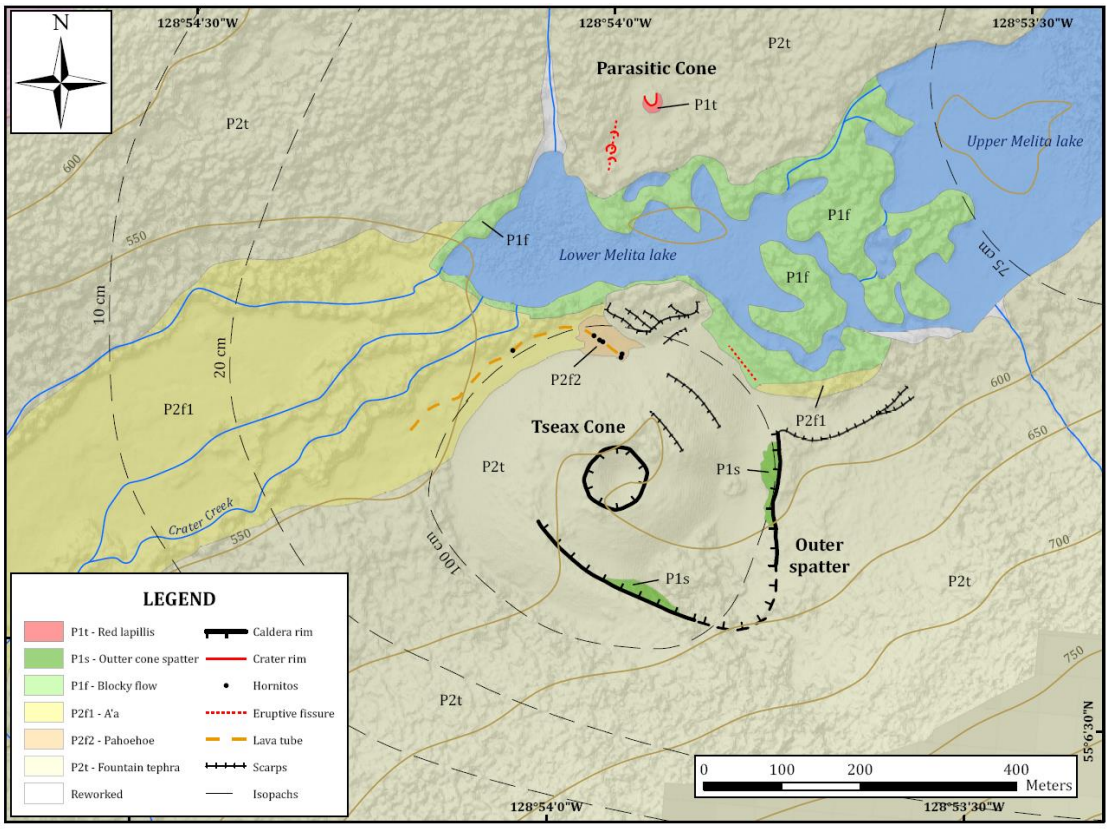

Figure 1.1 - Geologic map showing Tseax cone vent complex including the main cone, outer cone and parasitic cone (pers. comm. Le Moigne)

Tseax cone is associated with a 32 km long lava flow which follows topography from the main vent down into the Nass River Valley. The flow dammed both Crater Creek and the Tseax River leading to the formation of Upper and Lower Melita Lakes up-valley from the cinder cone, and Lava Lake at the confluence of Crater Creek and Tseax River (Fig. 1.2).

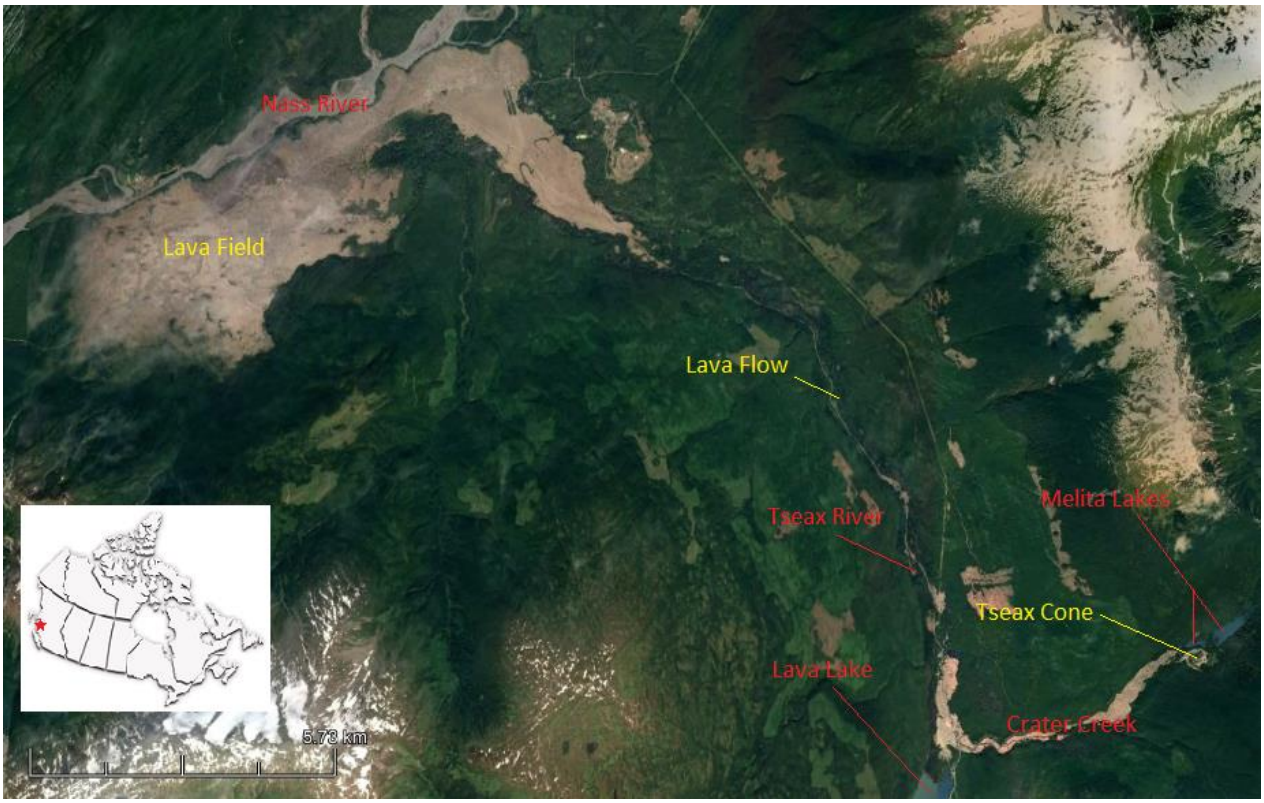

Figure 1.2 - Map showing Tseax Cone and the full extent of the lava flow. Inset showing location of Tseax in Canada.

The eruption of Tseax Cone has a single radiocarbon date of 250 ± 130 BP, based on a sample from a charred cottonwood tree (Lowden et al 1971). Tseax is therefore most likely the second most recently active volcano in Canada, after Lava Forks Flow. The Nass River Valley was inhabited at the time of the eruption by the Nisga'a people and Lowden's date accords well with Nisga'a accounts of the timing of the eruption. Two villages were said to have been destroyed by the lava flow and some 2000 people perished as a result of the eruption (Nisga'a Lisims Government, 2017). This casualty estimate is remarkably high to be associated with a mafic monogenetic volcano. The possible causes of death remain highly debated. The death of 2000 people would make the eruption of Tseax Cone the second deadliest natural disaster in Canada's history, after the 1775 Newfoundland Hurricane. The reported deadliness of this eruption makes understanding the eruptive history and processes at Tseax especially important, in order to better predict the hazards associated with similar eruptive settings.

This study investigates the pyroclastic deposits of Tseax Cone which have not previously been mapped or sampled. In this thesis I aim to provide a preliminary overview of the pyroclastic products of

Tseax, including their distribution, composition, and physical properties. These data are used to reconstruct the eruptive history of the explosive phase of volcanism, including the ordering of eruptive events and the style and scale of eruption. This is achieved using a combination of field mapping and sampling, componentry, grain size analysis, petrography, major and trace element geochemistry, modelling of ballistic trajectories and mathematical deposit volume estimation.

2. GEOLOGIC SETTING

2.1 Regional Geology

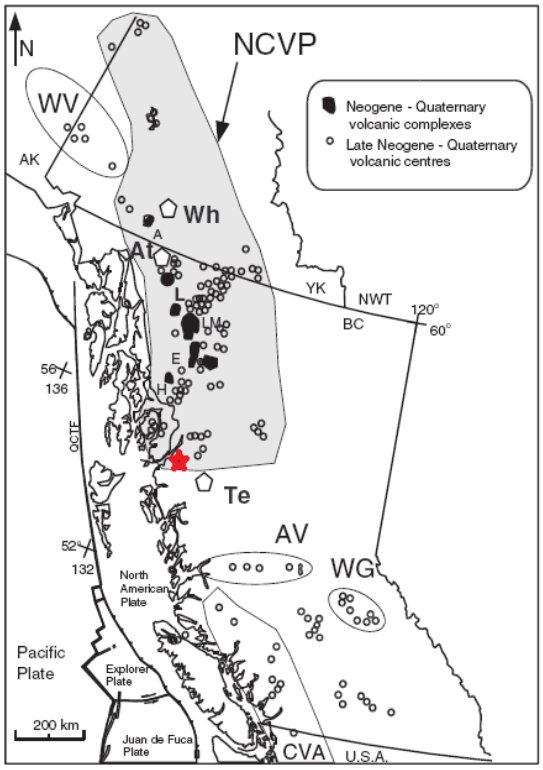

Tseax Cone is the southernmost eruptive center within the Northern Cordilleran Volcanic Province (NCVP). The NVCP is a region of Neogene to Quaternary volcanism, including more than 100 eruptive centers, that runs roughly parallel to the western edge of North America from northern British Columbia to the eastern edge of Alaska. The province is bounded by the Denali fault system on its western side and the Tintina fault to the east (Edwards and Russell 1999). Magmatism is linked to transtension and extension in the lithosphere due to interaction between the North American and Pacific Plates (Edwards and Russell 2000). Magmatism in this province has been ongoing since 20 Ma and Tseax and Lava Fork are the most recently active eruptive centers.

Figure 2.1.1 - Tseax Cone (red star) and the Northern Cordilleran Volcanic Province (NCVP) shown on a map of B.C. Adapted from Harder and Russell 2006

Cinder cones like Tseax Cone are common within the NCVP. Other volcanic landforms include volcanic plateaus, domes, and larger polygenetic volcanic centers and include both subglacial and subaerial forms. Magmas from the NCVP are predominately alkaline with alkali olivine basalt and hawaiite being the most common rock types. Basanites, which are prevalent at Tseax in addition to hawaiites, are also relatively common in the NCVP. Magmas in the NCVP are relatively Fe-rich and the

trace element compositions of most magmas are similar to that of Ocean Island Basalts (Edwards and Russell 2000).

Tseax is located at the southeastern edge of the Bowser sedimentary basin and the volcanic deposits overlie Late Jurassic Sediments of the Bowser Lake Group. In the region of the Nass River Valley the Bowser Lake Group consists primarily of a turbidite sequence of interbedded lithic arenites, and dark grey to black siltstones and mudstones. The Bowser Lake Group sediments are themselves underlain by Eocene granodiorites. The granodiorites are typically light grey to white and medium grained and are intruded by leucocratic dykes and veins of a variety of grain sizes (Van der Heyden et al 2000).

2.2 Previous Research

Previous studies of Tseax Cone have focused primarily on the lava, known as the Nass River or Aiyansh Lava flow. The lavas are easily accessible from the Nisga'a highway and display many unique features. Attempts have been made to characterize the surface morphology, petrology, geochemistry and age of the lava flow and several hypotheses have been proposed for the volcanic causes of the reported casualties.

The surface morphology of the lava flow is variable, including sections of blocky or rubbly a'a and level or tilted slabby pahoehoe. Brown (1969) classified the flow into six types of surfaces: level pahoehoe, tilted large slabs, bridge and collapse, small slab and block, blocky lava, and rubble of bombs and blocks. Some sections of the flow within the Nass River Valley contain regular and distinct pressure ridges of a few meters wavelength (Brown 1969). Other features of interest within the lava flow are lava tubes, tree casts, lava balls on the surface of the proximal region of the flow and megapillows where the distal edge of the flow is exposed along the Nass River.

Previous investigators have noted that the proximal and distal facies of the lava flow differ in their phenocryst content. The proximal portion of the flow, from the cone to the sharp turn in the flow at the confluence of Crater Creek and the Tseax River, is moderately to highly plagioclase-phyric, including some phenocrysts up to 1.5mm long, and poorly olivine-phyric. The distal portion of the flow by contrast is nearly aphyric and the few plagioclase phenocrysts that are present are much smaller, no longer than 0.5mm (Higgins 2009). Generally, the mineralogy of the lava flow has been found to include olivine, plagioclase and iron-titanium oxides both as phenocrysts and in the groundmass, while augite and accessory apatite are found exclusively in the groundmass (Nicholls 1982).

Major element data from samples of the Tseax lava flow has been published by Brown (1969), Hanson (1924), Erdman (1985), Nicholls et al (1982) and Nicholson (2008). These data show that the Tseax lavas are unusually iron rich, 13.11 to 16.00 wt % total Fe. The iron content is reflected in the high proportion of iron-titanium oxide minerals in both the phenocrysts and groundmass of the sampled lava (Nicholls 1982). Tseax magmas have been classified on the basis of silica and alkali content as basanites to hawaiites.

Previous studies have addressed the causes of the reported casualties associated with the Tseax eruption. Nisga'a oral histories indicate that those who died in the eruption, either while attempting to cross the Nass River or hiding in underground lodges, were killed by inhaling poisonous fumes before the lava flow reached their village (Barbeau 1935). A source of confusion is that it was the people of the village further from the vent, more than 20 km away, that were killed, while the village further up the Nass River were spared though their village was also destroyed. A Master's thesis produced by Nicholson proposes the hypothesis that the 2000 Nisga'a people reported dead were killed by a carbon dioxide gravity current released by the sudden overturning of a lake (Nicholson 2008). Nisga'a histories recorded by Barbeau (1935) indicate that prior to the eruption there was a foul smelling marshy lake present near to the lower village. Some versions of the legend of the eruption also indicate that rumbling was heard in the Crater Creek area for three years prior to the eruption (Barbeau 1935). If this was the case, Nicholson proposes that during this period of activity preceding the eruption of the lava flow CO_2 may have accumulated in the lake, only for the lake to suddenly overturn during the main phase of the eruption either due to accompanying seismic activity or due to sudden heating of the lake waters when the lava flow entered the Nass River. Other researchers have proposed that those escaping in canoes could have been killed by boiling of the river or swept away in a flood as the lava flow displaced the river, and that forest fires started by the lava flow could have resulted in some deaths (Nicholson 2008).

Although previous studies focused on the lava flow several past researchers also observed and photographed the main and outer cones. Most hypothesized that the outer cone was up to several hundred years older than the main cone and the lava flow, on the basis that it appears more eroded and vegetated. A single radiocarbon date was taken by Wuorinen (1978) from a piece of charred tree exposed in an eroded section of the outer cone to support this hypothesis. The date determined was 1325 ± 70 AD, 375 years before the lava flow (Wuorinen 1978).

3. FIELD CAMPAIGN

Tephra samples were collected and tephra thicknesses and ballistic locations were measured near Tseax cone in the Crater Creek valley, within Nisga'a Provincial Park, B.C., over a two-week period. Tephra thickness was mapped by digging holes with a shovel and measuring the depth to which lapilli deposits were observed while recording the location of the hole by GPS. Samples of the pyroclastic deposits were collected for later analysis from 30 of the holes.

Figure 3.1 – Holes dug at sites L2 (a digging location where no sample was taken) (left) and S22 (right). L2 was observed to the southeast of the main vent and shows a thin layer of lapilli between glacial tills and soil. S22 was taken on the flank of the parasitic cone and shows an upper black lapilli layer and a lower oxidized lapilli layer.

Sample locations are marked on Fig. 3.2. A single sample of tephra was taken at each of these sites except for S22 and S6 where two samples were collected at each locality. S22 and S6 were the only sites with two visually distinguishable layers, all other sample locations except for S5, showed a homogeneous layer of black lapilli with no discernable stratigraphy. S22 and S6 contained a black lapilli layer resembling the samples found elsewhere in the deposit overlying an oxidized layer. In S22 the lower lapilli were bright red and pervasively oxidized, while at S6 the lower lapilli where primarily externally oxidized and red-brown resembling the homogeneous deposit found at S5. At both sample sites the oxidized-unoxidized contact is sharp and approximately perpendicular to the ground surface. At many sites (Fig. 3.3, orange symbols), tephra thickness was greater than could be measured with our equipment and the maximum thickness observed was recorded. Seven main digging and sampling

traverses were followed with the aim of determining how tephra thickness decreased radially away from the main cone and of following the edge of the deposit where possible.

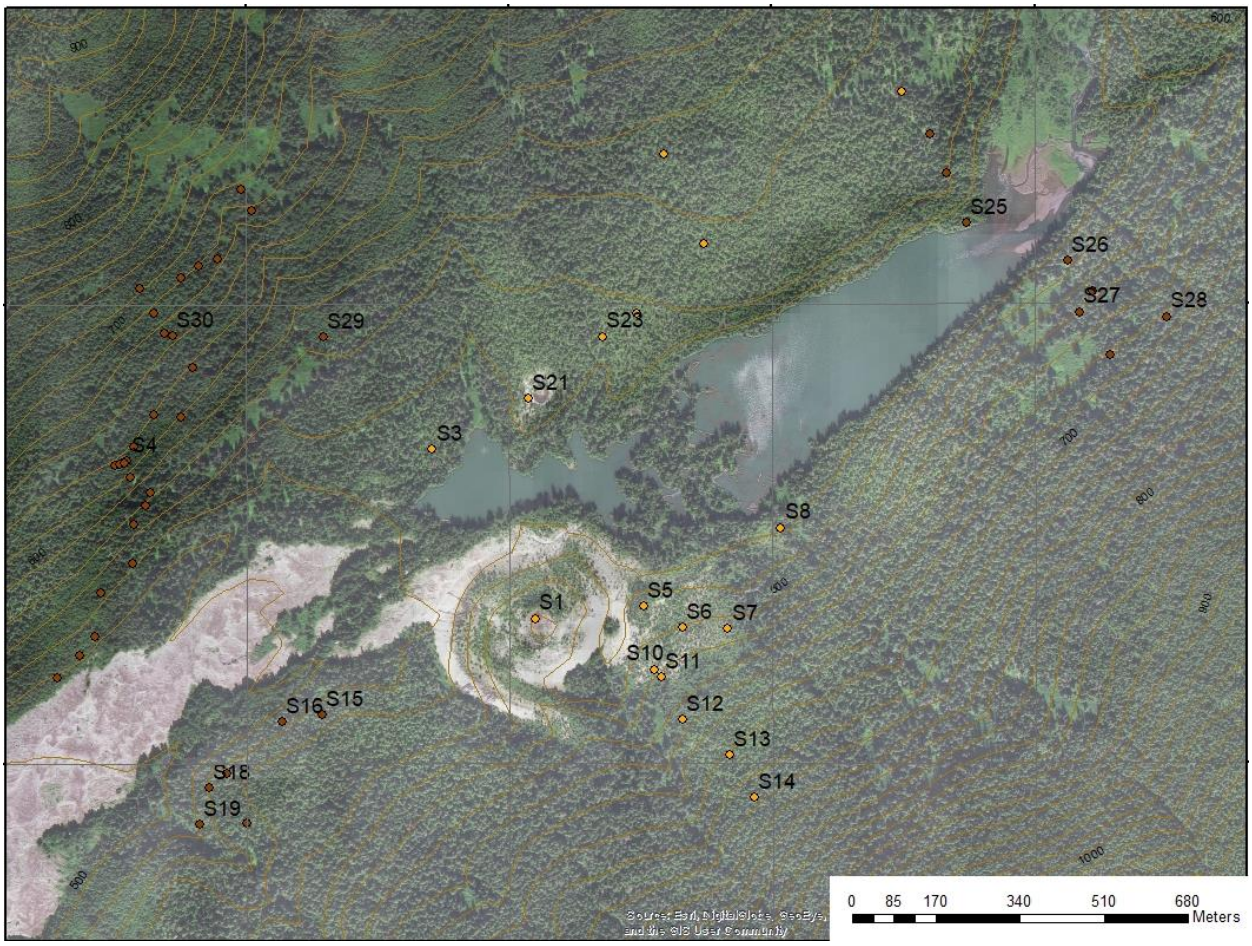

Figure 3.2 - Field map showing sample locations and labels

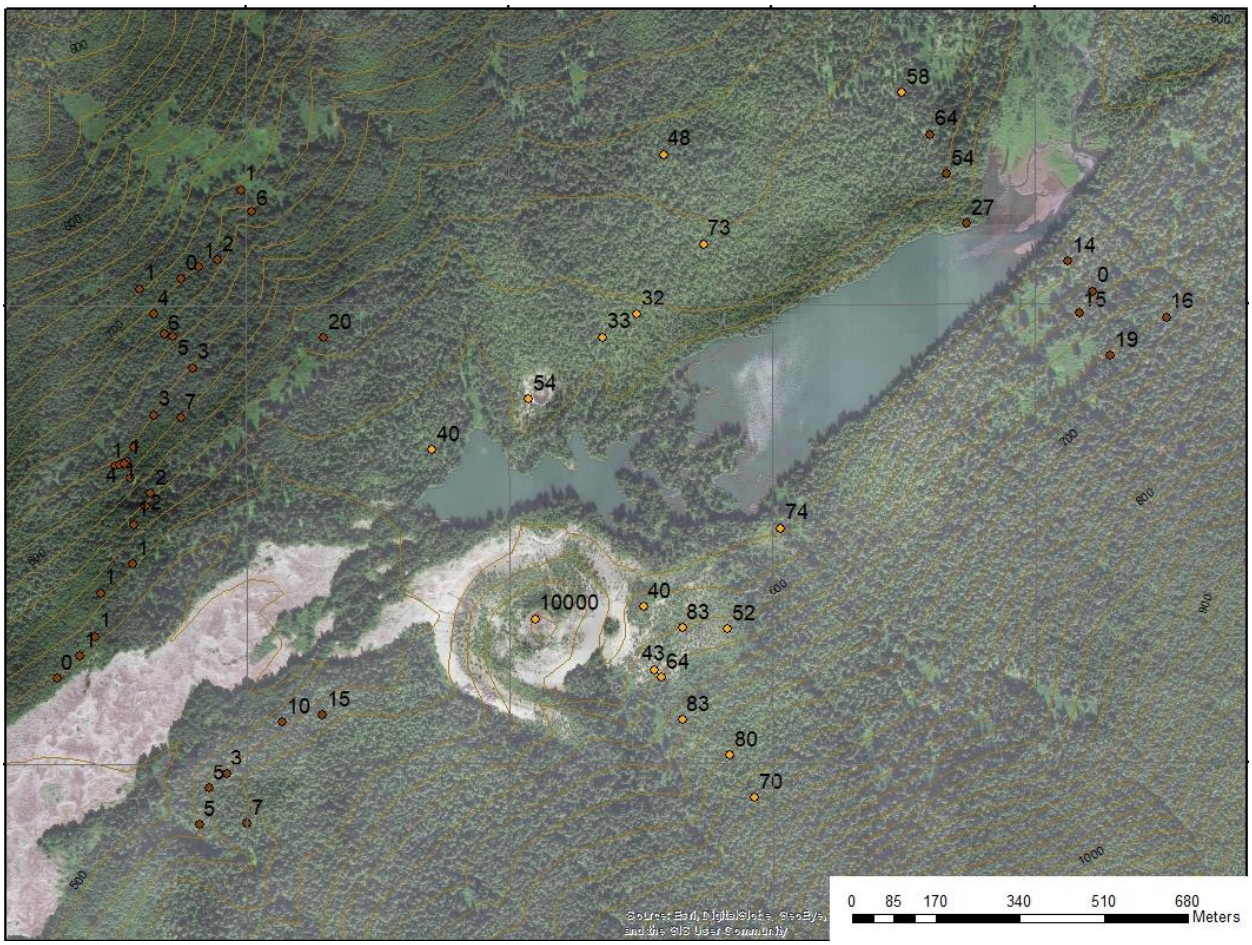

Figure 3.3 - Field map showing tephra thickness. Red points are known thicknesses, orange points are minimum thicknesses in cm.

Seventy-five volcanic bombs were GPS located and measured in three dimensions where possible. The locations of these bombs are marked on Fig. 3.5. Samples were taken from B2 and B7. The seventy-five measured bombs represent only a small fraction of the total observed bombs in the field area. In the proximal deposits where bombs were found at great density, bombs chosen for measurement were selected to approximately represent the range of sizes present.

Figure 3.4 – A typical oblate bomb B22 and a spindle bomb B59. Rock hammers for scale.

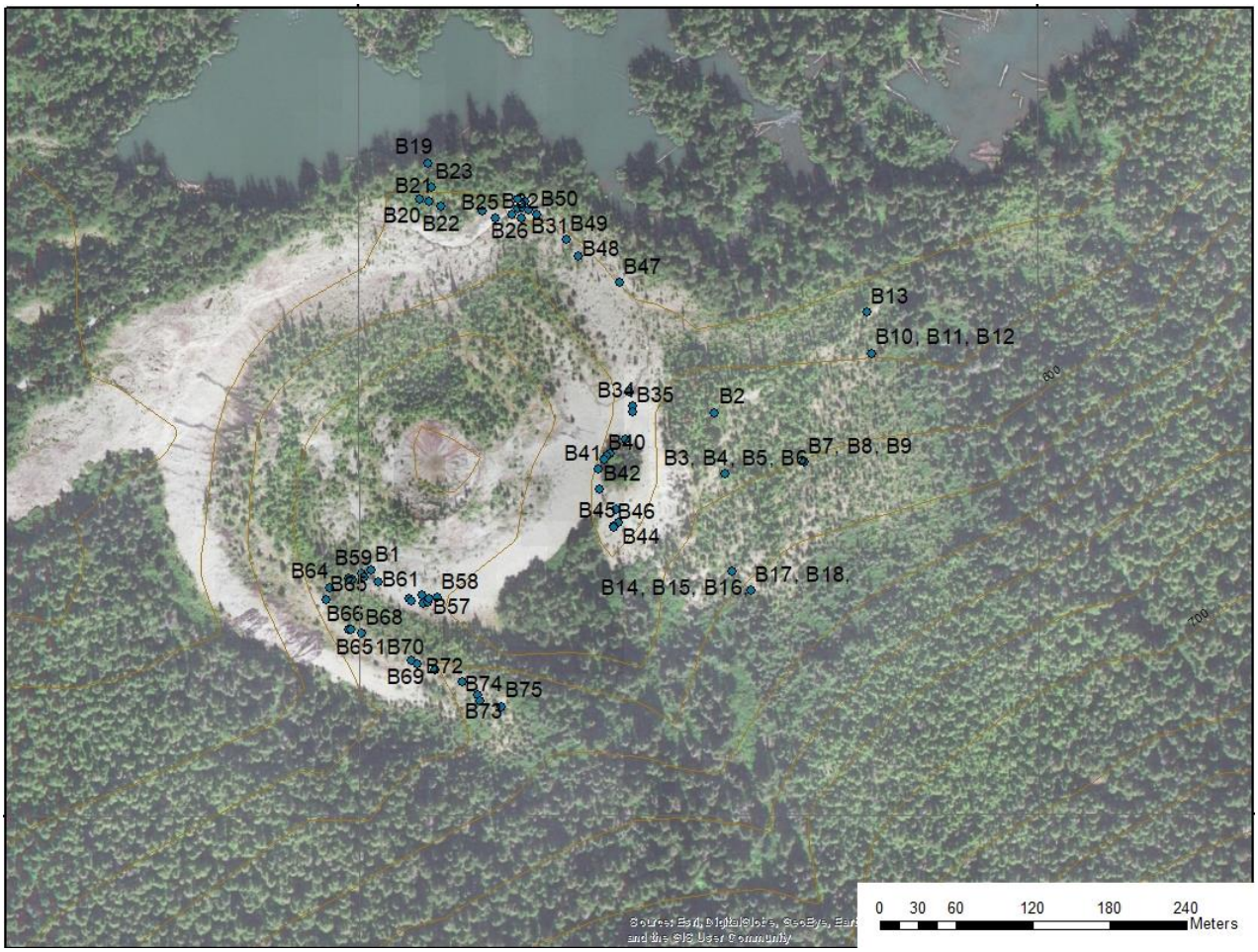

Figure 3.5 - Map showing locations 75 of measured ballistics

In several locations stratigraphic relationships were observed between the oxidized tephra of the parasitic cone, the black tephra of the main cone, the lava flow and the ballistics. At sampling sites S22 and S21, which were on the edge of the parasitic cone the black tephra layer found at most sampling sites overlay pervasively oxidized red tephra. The black tephra covered the flanks of the parasitic cone with decreasing thickness towards its summit where only red tephra was observed. When travelling on the proximal section of the lava flow we noted that no tephra was present on top of the flow, but a few ballistics were present. Ballistics were found in great abundance on top of the proximal tephra deposits and a few were found in the most proximal sampling holes. A small section of unoxidized spatter material was adhered to the dissected inner face of the southern section of spatter rampart. Another notable feature observed during our traverses was the occurrence of fluidal clasts up to 6 cm in size, dubbed 'Pele's bubble-gum', found at the summit of the parasitic cone and imbedded in the spatter of the outer cone at one location to the southwest of the main cone. Pele's bubble-gum were irregularly-shaped clasts featuring smooth or slightly wrinkled glassy surfaces showing very small or no vesicles but having a scoriaceous interior (Fig. 5.4.3).

Figure 3.6 - One of the largest 'Pele's bubble-gum' fluidal clasts observed. Collected at the summit of the parasitic cone. Author's fingers for scale

4. LABORATORY METHODS

4.1 Petrography

Two ballistic samples, B2 and B7, and two lapilli samples, S22a and S25, were made into polished thin sections at Vancouver Petrographics Ltd. The ballistics were first sliced using a rock saw and then marked with a white-out pen to select the best surface for the thin section. Small bags of lapilli of size fractions 2-4mm and 4-8mm from samples S22a and S25 were prepared and sent to Van Petro with instructions to create thin sections that maximized the number of lapilli that could be observed. These two samples were selected to represent an average black lapilli sample and a pervasively oxidized lapilli sample.

Five additional unpolished thin sections created for Dr. Jim Nicholls from the Tseax lava flow were obtained and analysed in addition to the new thin sections. Analysis of the thin sections was undertaken using a Nikon petrographic microscope. The volume percentage, shape and size of mineral phases and vesicles were recorded. The phenocryst and groundmass mineralogy were independently noted, and all thin sections were inspected for uncrystallised melt inclusions within the olivines for potential geochemical analysis. The polished thin sections of the pyroclastic materials were additionally inspected using reflected light microscopy to verify the mineralogy of oxide minerals observed.

4.2 Geochemistry

Seven lapilli samples and two ballistic samples were sent to ALS Geochemical Labs (North Vancouver, Canada) for analysis. The lapilli samples were selected from the 4-8mm size fraction of S6 upper and lower, S22 a and b, S5, S16 and S25. These samples were selected to represent different regions of the tephra deposits and both oxidized and unoxidized material. Interior samples of the two collected bombs B2 and B7 were sent. The samples were subjected to 14 element whole rock analysis by lithium borate fusion and XRF, quantification of carbon and sulfur by furnace combustion and quantification of ferrous iron. Samples S22a, S25 and B2 were additionally subjected to 30 element whole rock analysis by lithium borate fusion and ICP-MS (ME-MS81) to measure trace element concentrations. The Lower limit of reporting (LOR) for all major elements, as well as C and S was 0.01 wt%. The LORs for the trace elements analyzed are shown in Appendix C. No replicates or standards were included in this study, but error can be approximated for major and trace elements based on a set of 5 replicates also processed using XRF and ICP-MS at ALS Geochemical from a previous study by

Alexander Wilson. These replicates were of sample SH9315 from Cone Glacier, Iskut-Unuk Rivers Volcanic Center, B.C. and the errors are shown in Appendix D.

The ferrous iron measurements were used to determine separate weight percentages for FeO and Fe_2O_3 which are shown in Appendix A. The formula $Fe_2O_{3(R)} = Fe_2O_{3(T)} - (FeO_{(V)} / 0.8998)$ was used to determine the concentration of Fe_2O_3, which was then subtracted from the total to get the FeO concentration.

This data was combined with an unpublished geochemical dataset of Tseax eruptive materials produced by ALS for Yannick le Moigne, in 2017. The dataset included major and trace element concentrations for tephra, lava flow and spatter materials and was produced using the same procedures as were applied to my collected samples. Appendixes A and B combine both datasets and contain Major and Trace element data respectively.

4.3 Physical Properties

Pycnometry of sample cores taken from two ballistics, B2 and B7, was used to determine their skeletal density and connected porosity. The pycnometry was done according to the instructions in the AccuPyc II 1340 users manual. The cores were then weighed on a Sartorius balance to determine their mass. The skeletal volumes of the cores produced by the pycnometer were used with the masses of the cores to calculate skeletal density. Geometric densities were also calculated from the measured masses and the geometric volumes. Geometric volumes were determined by measuring the lengths and diameters of the cores using digital calipers. Skeletal and geometric densities were used to calculate the connected porosity of the cores according to

$$\varphi c = 1 - \frac{\rho geo}{\rho sk}$$

This was used to provide an estimate for the overall density and porosity of the Tseax ballistics.

4.4 Grain size analysis and componentry

Of the 30 lapilli samples collected, grain size analysis and componentry studies were performed on 12 samples selected to represent different domains of the tephra fallout deposits. These samples included: S5, S6 upper and lower, S8, S14, S16, S22 a and b, S23, S25, S28 and S29. The samples were cleaned by density separation to remove organic material. The samples were poured into buckets of

water and gently mixed so that organic materials would rise to the surface and could be scooped off. This was repeated until negligible organic material was produced by stirring. The samples were then allowed to settle so that the water could be gently poured off in stages while minimizing loss of fine ash. The samples were then placed in a low temperature oven to dry. This method was successful in removing organic contamination except for samples S16 and S23 which contained organic debris that did not float. Secondary effort was made to remove organic material manually from the wet samples, but some contamination remained in the 1-2mm and smaller size fractions. Samples S14, S16, S23, S25, S28 and S29 contained lapilli which floated on water and these were separated and cleaned manually.

Dried samples were sieved using a standard set of sieves with mesh spacings of 63mm, 32mm, 16mm, 8mm, 4mm, 2mm, 1mm, 0.5mm, 0.25mm, 0.125mm and 0.063mm. Floating and non-floating clasts were sieved separately for each sample so that their relative proportions could later be estimated as part of componentry. Each size fraction was then weighed using a Sartorius, Ohaus Scout Pro, or Ohaus Explorer Pro balance for samples of increasing total weight. Weights are understood to be accurate to 4 significant figures for all samples. Weights were normalized to weight percentages and cumulative weight percentages. These data were plotted as a histogram of weight percentages and a cumulative weight curve. The cumulative weight curves were additionally plotted all on one graph for comparison. Inman parameters were then calculated for each sample.

Componentry of the 12 samples was undertaken using a Fisher Scientific Stereomaster microscope to observe the clast types (juvenile material and lithics) and geometries found in each sample. Componentry was described for each size fraction of each sample and plotted as a histogram.

4.5 Isopach mapping and volume estimation

Absolute and minimum tephra thicknesses were plotted on a map of the field area as shown in Fig 3.2 and used to develop an isopach map. Initial attempts to draw an isopach map produced a pattern of thinning towards Melita Lakes and Crater Creek in the center of the valley which gave the appearance of two plume axes. Grain size analysis was incorporated to determine if this thinning was a result of erosion, overthickening or reduced initial deposition. The relative proportion of fines was used as a proxy for distance to the initial edge of the deposit. The grain size data was interpreted to indicate that thinning towards the center of the valley was a product of erosion and not plume behavior. Therefore, the measured thicknesses in the eastern portion of the map were treated as minimum thicknesses when

the isopachs were drawn. The isopach map was drawn by hand on a printed map of tephra thickness data points produced on ArcGIS.

Approximate volume estimates for the deposit were calculated by summing the volumes of all the defined isopachs. The paper within each isopach, when the map was scaled to a single sheet of printer paper, was weighed using a Sartorius balance to determine the ratio of the isopach's weight to the total sheet weight. The area of each isopach was then calculated from this ratio and the total area of the sheet. The isopach areas were multiplied by their minimum thickness value to determine their volumes. For the 0 cm isopach a thickness of 0.1 cm was designated. For the area occupied by the cone itself an approximate volume was calculated using the formula for a truncated cone, with crater and base radii determined on the ArcGIS base map and the height determined by Le Moigne (pers. comm.) from elevation profiles.

Based on the extreme uncertainty of the isopachs it was determined that more accurate calculus or modelling based methods for estimating volume would not contribute significantly to the accuracy of the output. The volume value obtained was compared to an estimate produced using a simple formula relating crater diameter and total tephra volume from Sato and Taniguichi (1997). This method uses the equation

$$D = 0.11\ V^{0.42}$$

for magmatic eruptions. Crater diameter was estimated by taking the average of fived measured diameters across the crater of the main cone on the ArcGIS basemap.

4.6 Ballistic Trajectory Analysis

Eject! (Mastin 2008), a ballistic modelling software was used to constrain the energy required to transport ballistics from the vent of Tseax cone to their locations at various distances from the vent. Eject! Is designed such that single values for drag coefficient, block shape, block diameter, density, vent elevation, temperature at sea level, tailwind speed, total loss of elevation from the vent to location of ballistic landing, zone of reduced drag, ballistic exit velocity and ejection angle are input. Each run can produce a maximum of five outputs and the expected output for Eject! is a graph of the trajectory of a ballistic, given as plot of vertical versus horizontal distance travelled.

Drag coefficient and block shape were estimated using the prescribed values from Crowe et al. (2009). This estimate was based on visual inspection of photographs of the ballistics, and the ratio of the maximum, intermediate and minimum diameters of ballistics measured in the field. Field measurement of ballistics provided values for the diameter of 74 ballistics ejected from Tseax cone. The density was set at 910 kg/m^3, the average density of the two ballistics, B2 and B7, that were sampled and cored. Elevation at the vent was set at 609 m based on Google Earth elevation profiles. Temperature at sea level was set at 15°c. This is the approximate median temperature over the last 16 years of weather data during the late summer to fall in nearby Terrace (Weather Network, 2017). The season was selected based on Nisga'a oral histories describing the eruption of Tseax Cone, which recall that it occurred during salmon spawning (Barbeau, 1935). Tailwind speed was set at 4.5 m/s for ballistics to the East and North of the vent, the downwind directions during the eruption based on the geometry of the tephra deposit, and 0 km/h for ballistics to the South of the vent. The windspeed value is an approximate average of windspeeds recorded in 1955 to 2014 climatic data, also collected in Terrace by Environment and Climate Change Canada (Environment and Climate Change Canada, 2017). The windspeeds were then were adjusted to account for the angle of the ballistic path relative to the predominant wind direction, as determined from the asymmetry of the tephra deposit. Elevation loss and zone of reduced drag were ignored and set to zero for simplicity. The distances of the individual Tseax ballistics from the vent, to which the outputs of the two programs were compared, were determined from their respective GPS coordinates, using Movable Type Scripts website (Veness, Calculate distance, bearing and more between Latitude/Longitude points).

A single value was used in all runs for drag coefficient, block shape, vent elevation, temperature, and block density. 74 specific combinations of diameter and windspeed were input to represent real scenarios based on the dimensions and positions of measured ballistics. Ejection angles of 10, 15, 25, 35, 45, 55, 65 and 75 degrees from horizontal were tested for each ballistic to encompass the range of angles which Eject! can effectively model. Ballistics travelling at angles outside of this range would fail to exit the vent. Exit velocity was then varied for each ejection angle until a horizontal distance corresponding to the real distances of ballistic from the vent was produced. The angle and velocity pairs were then recorded and plotted for each ballistic.

5. LABORATORY RESULTS

5.1 Petrography

Thin sections of Tseax eruptive materials including bombs, coherent lava and unoxidized and oxidized tephra were uniform in their mineralogy. All samples included phenocrysts of plagioclase, olivine and magnetite. Lava sample NR-10 also contained a cluster of clinopyroxene phenocrysts of maximum 1mm diameter. The phenocrysts of plagioclase and olivine in the bombs and lava were often observable in hand sample being up to 2.5mm in their maximum diameter. The phenocrysts in the tephra however were only observable in thin section and were an average of 0.1mm in diameter. In all samples plagioclase was the dominant phenocryst type. Phenocrysts were subhedral to euhedral. Both tephra samples and bomb B7 included phenocryst sized xenoliths of a laminated siltstone.

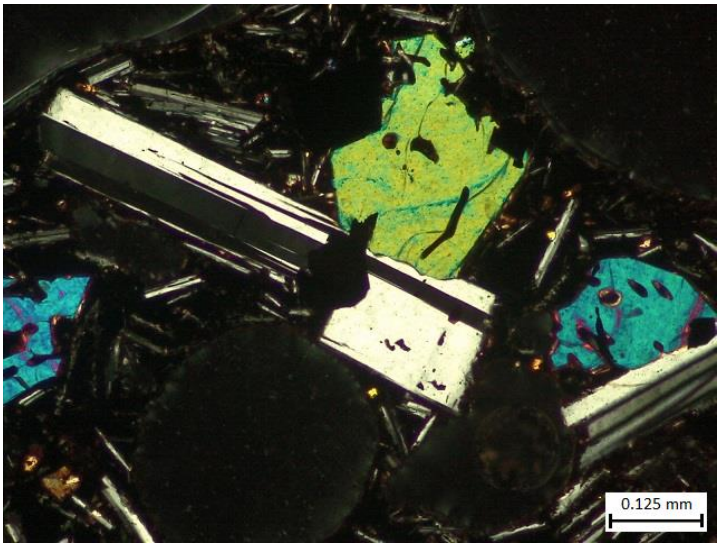

Figure 5.1.2 - Petrographic image of typical phenocryst geometries in bomb B2 in XPL

The groundmass of the tephra samples is composed exclusively of glass. The lava samples are hypocrystalline, and the bomb samples are intermediate between the two having a hypohyaline groundmass containing plagioclase microlites, and a few olivine crystals in B2. The groundmass of all the lava samples consisted of plagioclase, olivine, magnetite, clinopyroxene, fine elongate crystals of a second oxide interpreted to be hemo-ilmenite, apatite, and minor interstitial glass.

All samples were vesicular with the bombs and tephra having a significantly higher volume percentage of vesicles than the lava. The vesicles of the lava flow samples were generally isolated, except for in NR-1B which had a few clusters and chains of vesicles. In NR-7, NR-8 and NR-9 the vesicles were small, less than 1 mm in diameter. NR-1B had vesicles up to 3.5 mm diameter and NR-10 had the largest vesicles, including one that was 8 mm in diameter. The vesicles ranged from highly irregular in NR-7 and NR-8 to moderately irregular in NR-9 and NR-1B and rounded in NR-10. The bombs contained the largest vesicles, up to 8mm, which were rounded and often connected with one or more neighboring vesicles. The vesicle size of the tephra samples was constrained by the size fraction chosen for the thin section. Vesicles were up to 1.8mm in diameter, round and isolated, despite only having very thin walls between them in many lapilli. Vesicularity varied significantly between individual lapilli.

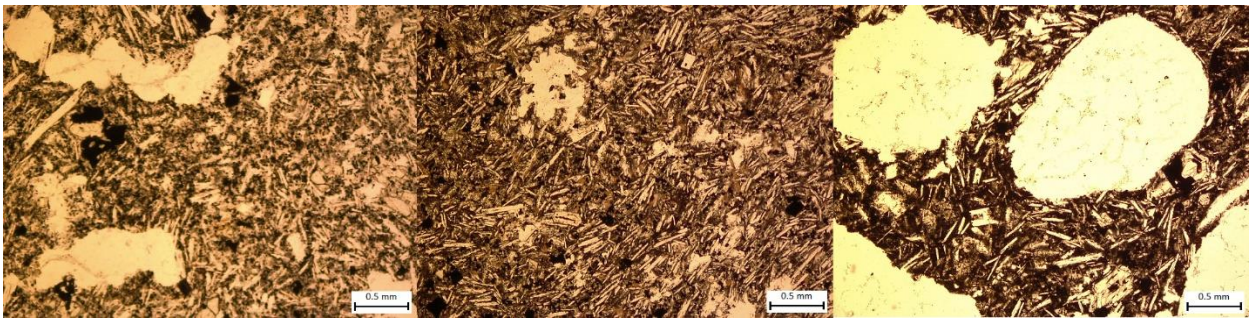

Figure 5.1.3 - Petrographic images showing vesicle geometries in lava samples. From left to right: NR-1B moderately irregular connected vesicles, NR-7 highly irregular isolated vesicles, NR-10 larger, rounded isolated vesicles. In PPL.

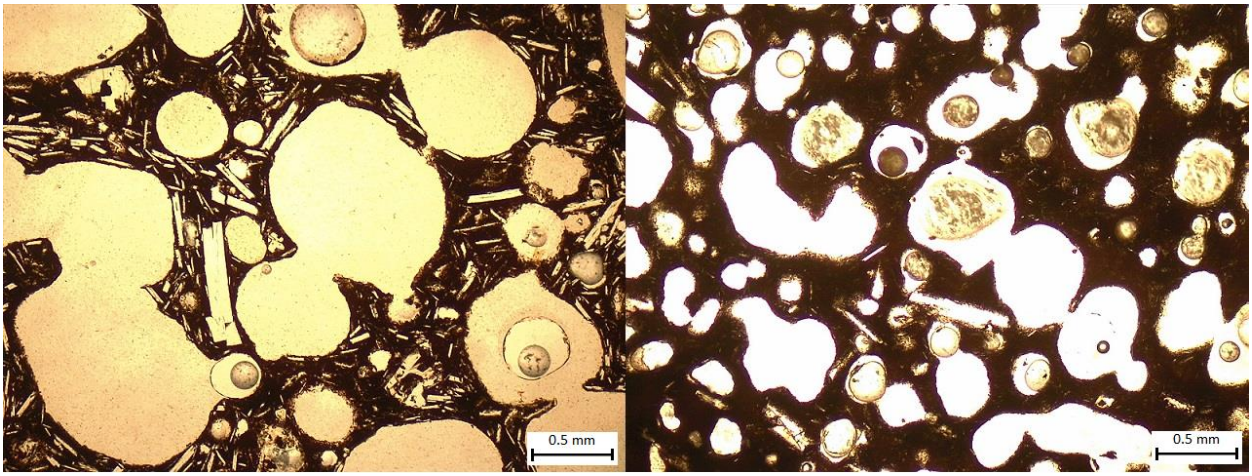

Figure 5.1.3 - Petrographic image showing vesicle geometries in bombs: left: B2, right: B7, in PPL.

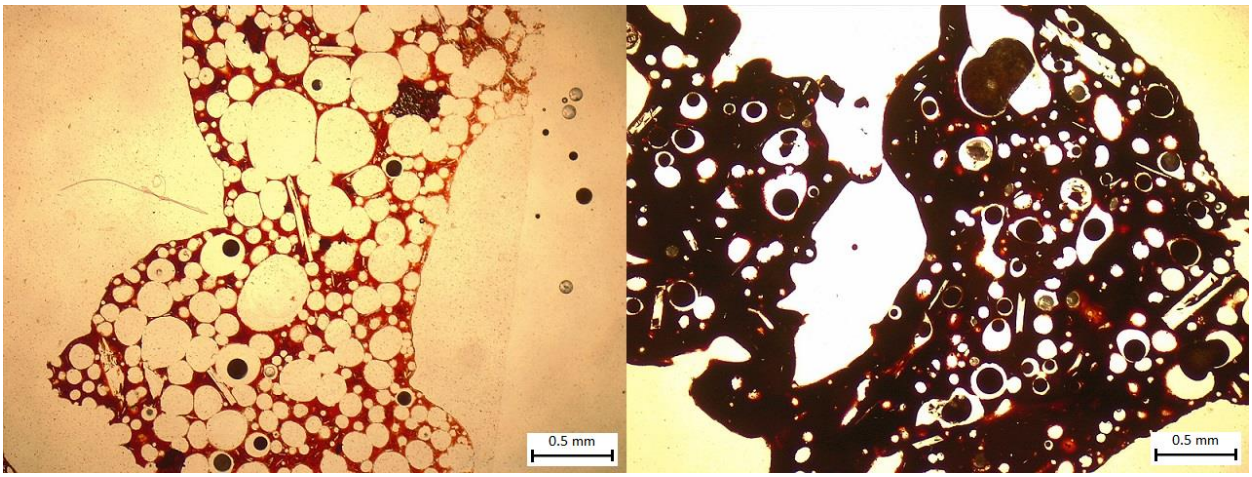

Figure 5.1.4 - Petrographic images showing range of vesicularity in lapilli. Both images are from S22a in PPL.

5.2 Geochemistry

Major element data was used to produce a TAS diagram showing the compositional names for all sampled materials. The Tseax Cone samples fall within the compositional ranges of basanite, trachy-basalt and basalt based on a Total Alkali and Silica plot (Fig. 5.2.1). The samples fall within a narrow

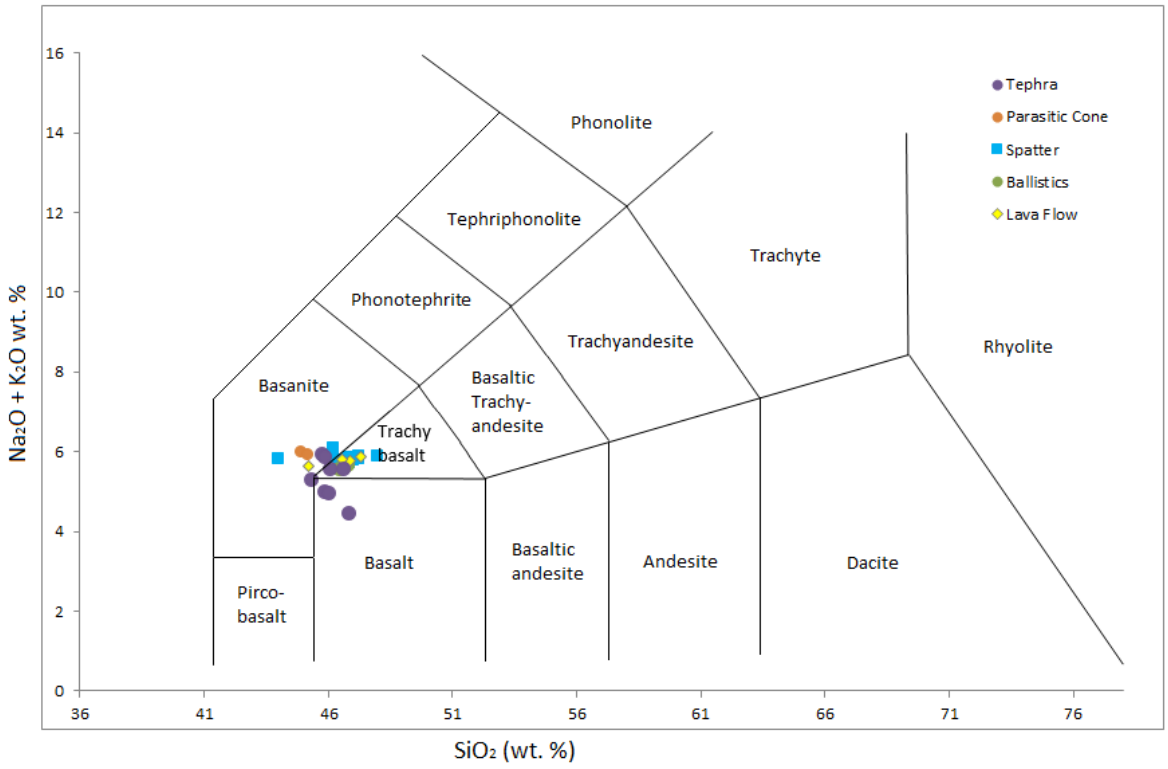

Figure 5.2.1 - Total Alkali Silica diagram of all juvenile Tseax samples

range of 45.80 to 48.00 wt % SiO_2 and 4.45 to 6.79 wt% alkalis. All eruptive material types include some samples classed as trachybasalts and all materials except for the ballistics include basanites. Only the unoxidized tephra samples fall within the basalt field. Trachy-basalt samples are further described as hawaiites because their wt. % Na_2O - 2 is greater than their wt. % K_2O.

Trace element data was used to produce a standard trace element concentration plot with concentrations normalized against primitive mantle values determined by Sun & McDonough (1989). Concentrations of Sn and W were provided by ALS but excluded from the analysis because their LORs were too high relative to the values produced. Trace element compositions for all types of Tseax samples are highly uniform. Fig. 5.2.2 shows the average compositional trends for oxidized and unoxidized tephra, bombs, spatter and coherent lavas. The only minor variance between the trends is in the Cs content. The oxidized tephra from the parasitic cone are noticeably enriched in Cs compared to the other eruptive materials. This difference can probably be attributed to the mobility of Cs as a Large Ion Lithophile element; Cs may have entered the parasitic cone samples during the oxidation process. The trends are additionally compared to OIB values from Sun & McDonough (1989). The trends for Tseax materials match the Ocean Island Basalt (OIB) trend well except for being highly enriched in Ba, showing that Tseax magmas are most likely derived from a similar asthenospheric source as OIBs but have assimilated some crustal material prior to erupting.

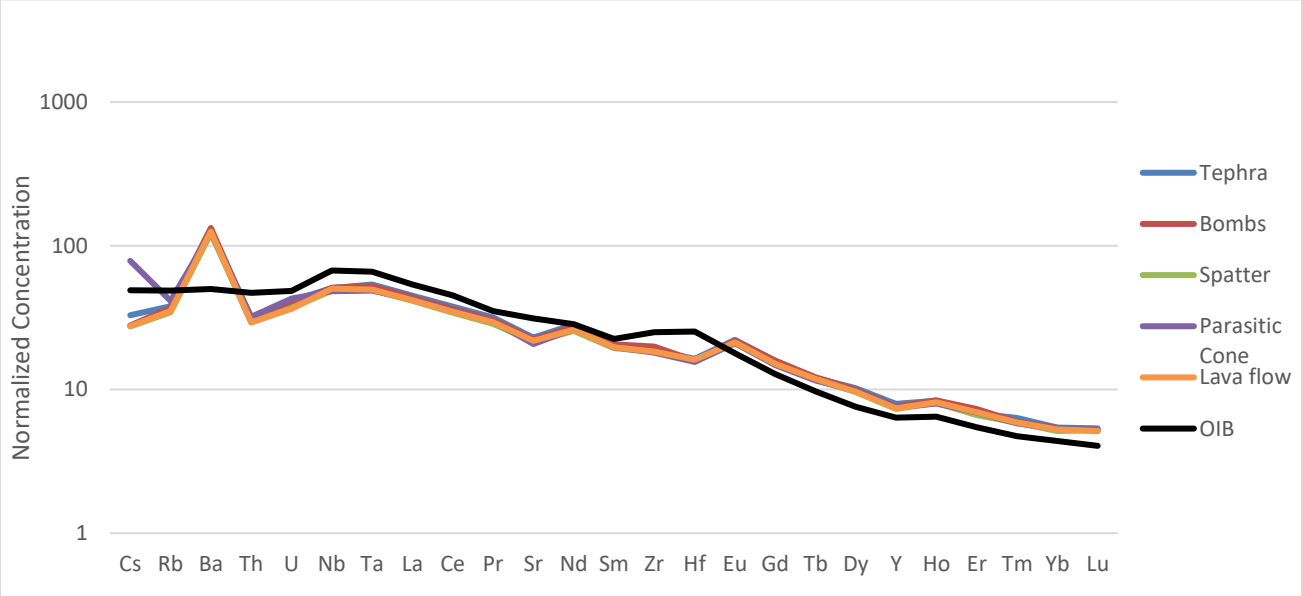

Figure 5.2.2 - Trace Element plot showing concentrations normalized to Primitive mantle (Sun and McDonough 1989) for Tseax eruptive materials and OIB

5.3 Physical Properties

Measured ballistics produced an average skeletal density of 2.92 ± 0.01 g/cm^3 and an average geometric density of 0.909 ± 0.05 g/cm^3. The ratio of these values produced an average connected porosity of 68.9%. This is slightly larger than the estimated volume percentage of vesicles in the bomb thin sections. It is therefore assumed that there is very little isolated porosity in the bombs.

A fraction of the unoxidized tephra float on water and thus are assumed to have a geometric density of less than 1.00 g/ cm^3. The most vesicular lapilli observed within thin-section S25, which were assumed to be the floating clasts, had vesicle volume percentages of 60% to 85%. This is compared to the ballistics which had vesicle volume percentages of 50% and 65%. The average geometric density of the ballistics was less than 1.00 g/ cm^3 but their porosity was inferred to be primarily connected. If the skeletal densities of the ballistics and tephra are assumed to be similar, then the lapilli would need to posses at least the same vesicularity as the bombs but have primarily isolated vesicles. Thus, a minimum of 50% of the volume of the lapilli would need to be occupied by isolated vesicles, but an additional up to 35% of the volume would consist of connected vesicles in the floating lapilli samples.

5.4 Grain size analysis

Grain size distribution shows limited variation between the proximal and distal sampling sites. All samples analysed are dominated by the 4-8mm size fraction. The proportion of the sample found within this size fraction, for the unoxidized samples, generally increases with distance from the main vent. No similar trend is found within any other size fraction and there is no noticeable difference between the proximal and distal samples in terms of their percentage of the finest or coarsest size fractions.

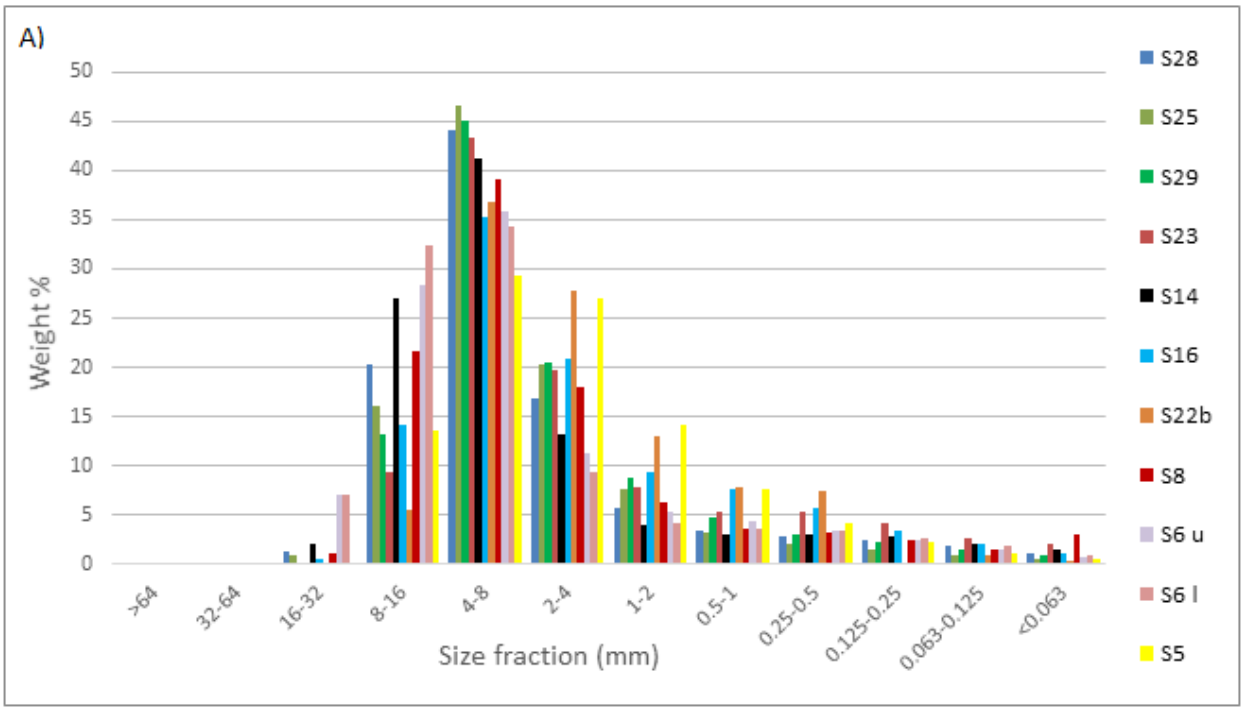

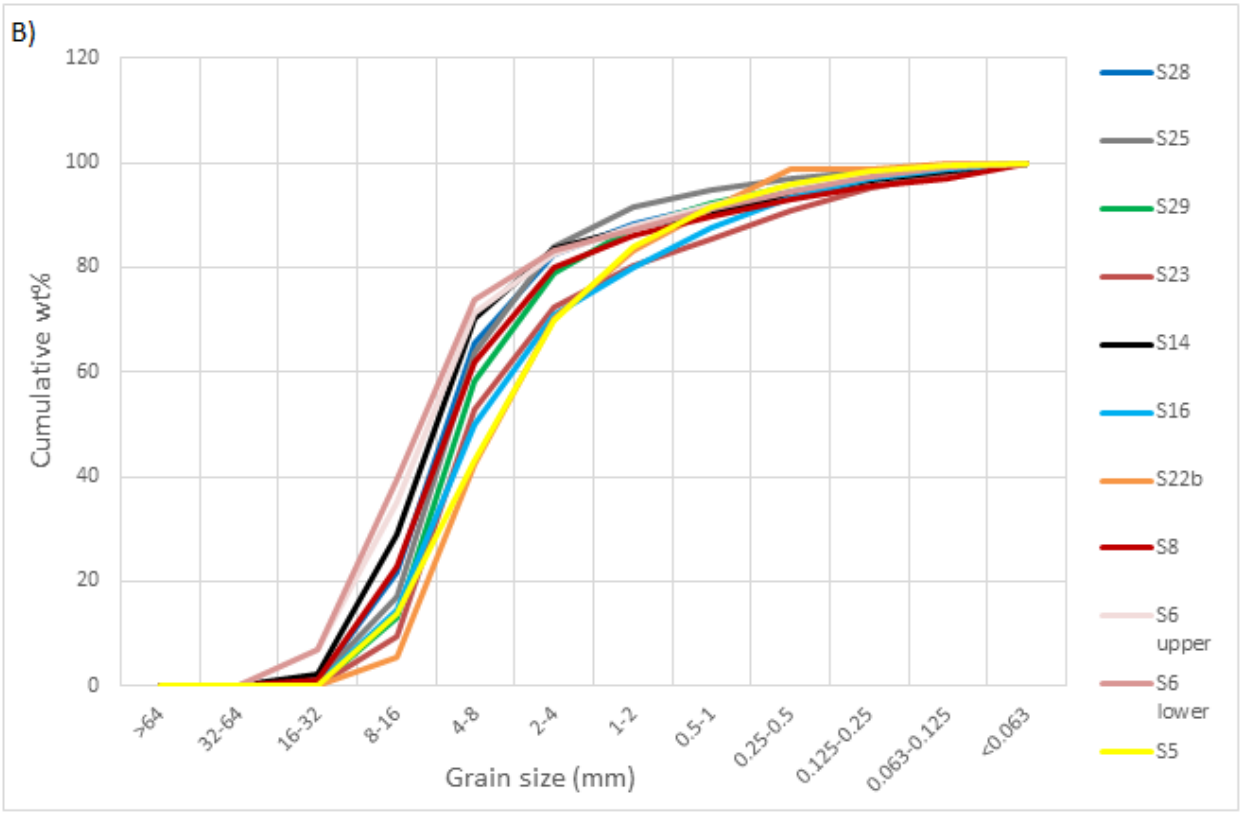

Figure 5.4.1 - Grain size distribution for samples from the main tephra deposit ordered from distal to proximal. A) grain size distribution B) cumulative weight curves

Samples are well sorted or very well to well sorted, as determined using Inman parameters (Fig 5.4.2). There is no distinct correlation between distance from the main vent and any Inman parameter.

Sample	16φ	84φ	Md (φ)	αφ	σ (φ)	Sorting
S5	-2	0	-1	-0.5	1	very well - well sorted
S6 lower	-3	0	-2	-0.5	1.5	well sorted
S6 upper	-3	0	-2	-0.5	1.5	well sorted
S8	-3	0	-2	-0.5	1.5	well sorted
S14	-3	0	-2	-0.5	1.5	well sorted
S16	-2	1	-1	0	1.5	well sorted
S22a	-2	-1	-3	-1	1	very well - well sorted
S22b	-2	1	-1	1.5	1.5	well sorted
S23	-2	1	-2	1.5	1.5	well sorted
S25	-2	1	-1	1.5	1.5	well sorted
S28	-3	0	-2	1.5	1.5	well sorted
S29	-2	0	-2	1	1	very well - well sorted

Table 5.4.2 - Inman parameter values for eleven samples from the main tephra deposit and one sample from the parasitic cone (S22a)

Within the samples analysed six types of juvenile components and three types of accessory lithics were defined. Juvenile components include: black or brown scoriaceous lapilli (glass shards at the finer size fractions), pervasively oxidized red scoriaceous lapilli, externally oxidized red-brown scoriaceous lapilli, black pumiceous lapilli, black fluidal clasts and oxidized fluidal clasts. Black or brown lapilli dominate all samples examined except for S5, S6 lower and S22a. S5 and S6 lower were dominated by externally oxidized lapilli and were collected in sampling locations proximal and to the Southwest of the main cone. S22a is dominated by pervasively oxidized lapilli and was collected from the parasitic cone. S22a contains some black lapilli, and likewise S22b contains some pervasively oxidized lapilli, probably as a result of contamination during digging. Floating lapilli were found in S16, S23, S25, S28 and S29, representing proximal and distal regions of the deposit. The black fluidal clasts were found in all samples except for S5 and S22a. Oxidized fluidal clasts were found in S5, S22a and S22b. The fluidal clasts include Pele's spheres and smaller versions of Pele's bubblegum.

Accessory lithics included: beige to dark grey platy siltstones and mudstones, cream coloured fine grained porphyroblastic metamorphic clasts and cream and black fine grained phaneritic plutonic clasts. The siltstones and mudstones were the most common lithic; they were present within multiple size fractions and at volume percentages of up to 12.5 %, but usually not more than 0.5 %, in all samples

except S5 and S22b. The metamorphic lithics were found only in S6 upper and lower and S29 and were usually represented by just a few individual grains in the entire sample. The plutonic lithics were found only in the 1-2 mm size fraction of S25 and only two individual grains were observed.

5.5 Volume Estimation

A very approximate isopach map was drawn based on the absolute and minimum tephra thicknesses measured in the field (Fig. 5.5.1). The deposit is elongate to the northeast indicating a plume that was significantly affected by winds from the southwest. The total area included within the isopachs was approximately 2.2 x 10^7 m^2. The volume produced using the sum of the estimated isopachs was approximately 6.1 x 10^6 m^3. This should be understood to be a minimum value for the tephra volume. The average volume produced by the crater diameter method was 2.17 x 10^6 m^3 with a range from 1.82 x 10^6 m^3 to 2.44 x 10^6 m^3.

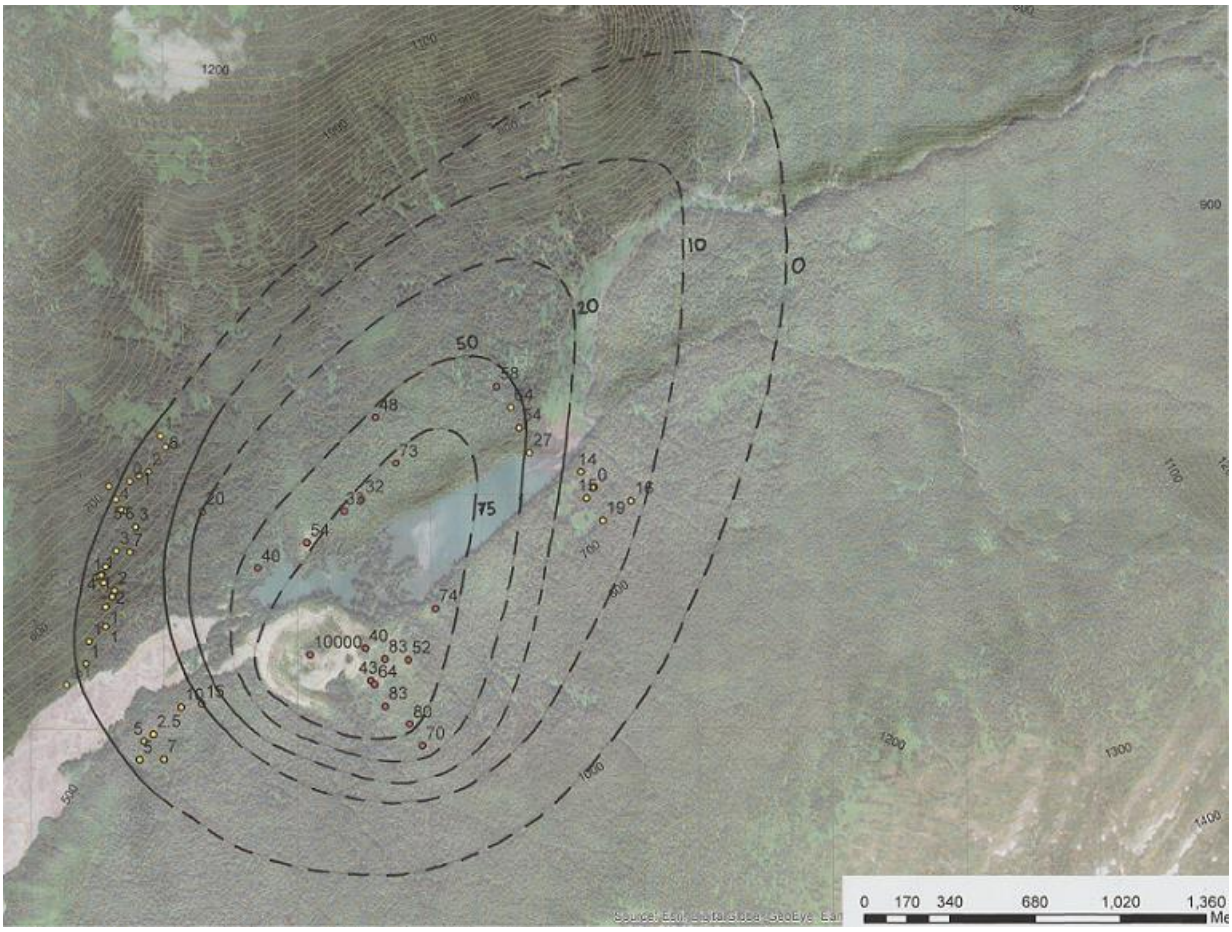

Figure 4.5.1 - Isopach map with isopach lines representing minimum thicknesses in meters

5.6 Ballistic Modelling

Modeling with Eject! was used to produce possible ejection angle and exit velocity combinations for Tseax ballistics to determine a feasible range of velocities. Generally, the larger the minimum exit velocity required for a ballistic to reach its location the greater the difference between the exit velocities needed for low and high ejection angles.

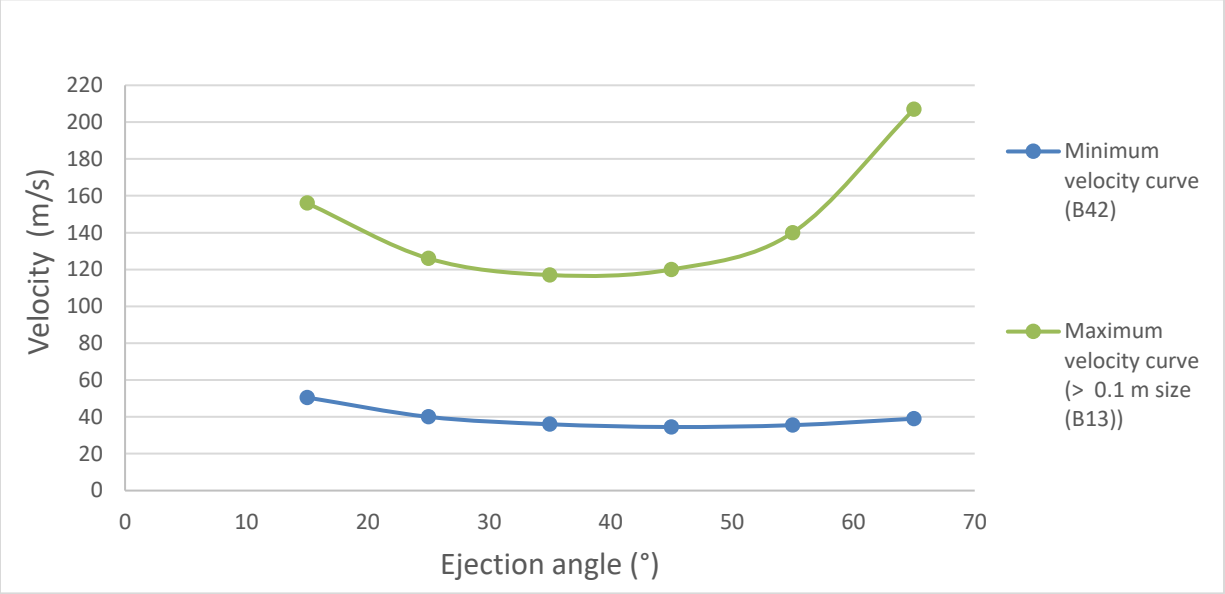

Figure 5.6.1 - Plot showing minimum and maximum velocities curves for measured Tseax ballistics

The minimum velocities predicted for the modelled Tseax ballistics were for a large ballistic (B42) with a median diameter of 0.58 m which was located 125 m from the vent. The model predicted that the minimum velocity at which this ballistic could have travelled was 34.5 m/s if ejected at a 45° angle, and the maximum velocity it may have travelled at was 62 m/s if it was ejected at a 10° angle. The maximum velocities were associated with the smallest collected ballistic (B8), which had a median diameter of 0.08 m, and was measured 282 m from the vent. The model predicted that to reach the location it was collected B8 would have needed a minimum exit velocity of 265 m/s with an ejection angle between 25° and 35°. The maximum modelled velocity was 520 m/s at 55°. The program was not able to model a scenario for ejection angles greater than 55°. However, ballistics smaller than 10 cm in diameter are thought to be affected by plume dynamics (Bertin 2017). Therefore, the second highest velocity ballistic modelled (B13), which had a diameter of 19 cm was taken to represent the highest

velocity true ballistic trajectory. Eject! predicted that B13 would have travelled at a minimum of 117 m/s at an angle of 35° or a maximum of 610 m/s at 75°. All other ballistics tested showed minimum and maximum predicted velocities intermediate between B13 and B42 and therefore the velocity curves of these two ballistics are used to delineate the range of feasible velocities.

The range of feasible velocities was designated as the realm between the curve for B13 and B42 from ejection angles of 15° to 65°. This is intended to represent a reasonable range of angles that would allow the ballistic to exit the vent without encountering the side or falling back in, and to eliminate an extreme value of 610 m/s for B13 at 75° which is outside the typical range for volcanic ballistics (Taddeucci et al 2017). These restrictions provide a total velocity range of 34.5 m/s to 207 m/s. These values are typical for ballistics associated with Strombolian eruptions and would be considered energetic for Hawaiian eruptions (Taddeucci et al 2012, Larsen et al 2007).

6. DISCUSSION

6.1 Time constraints on the eruptive history

The overall petrographic and geochemical homogeneity of sampled Tseax eruptive materials, including coherent lavas, unoxidized tephra from the main cone and tephra deposits, spatter from the outer cone and oxidized tephra from the parasitic cone, point towards a single magma batch as the source for all of the volcanic features associated with Tseax Cone. New unpublished paleomagnetism data collected in association with this study indicate that the lava flow and the spatter material from the outer cone have magnetic orientations that differ by less than 0.33° with a maximum error of 2.5° (pers. comm. Rene Barendregt). This indicates that the lava flow and spatter cone were likely formed within the same year. These lines of evidence, in addition to the position of the main tephra cone within the outer spatter cone supports a hypothesis that all the volcanic products at Tseax Cone were produced as part of a single eruptive event. This is contrary to previous hypotheses that the outer cone formed approximately 375 years prior to the main cone (Wuorinen 1978).

Major element data from the samples analyzed at ALS was compared to pre-existing geochemical data on the lava flows from Brown (1969), Hanson (1924), Erdman (1985), Nicholls et al (1982) and Nicholson (2008). These data are compiled in Appendix E. When plotted on a TAS diagram the published data fell within the same compositional categories as the new lava flow data, including

basanites and hawaiites. These data were very slightly enriched in both silica and alkalis compared to the new data on average, but the two data sets overlapped significantly.

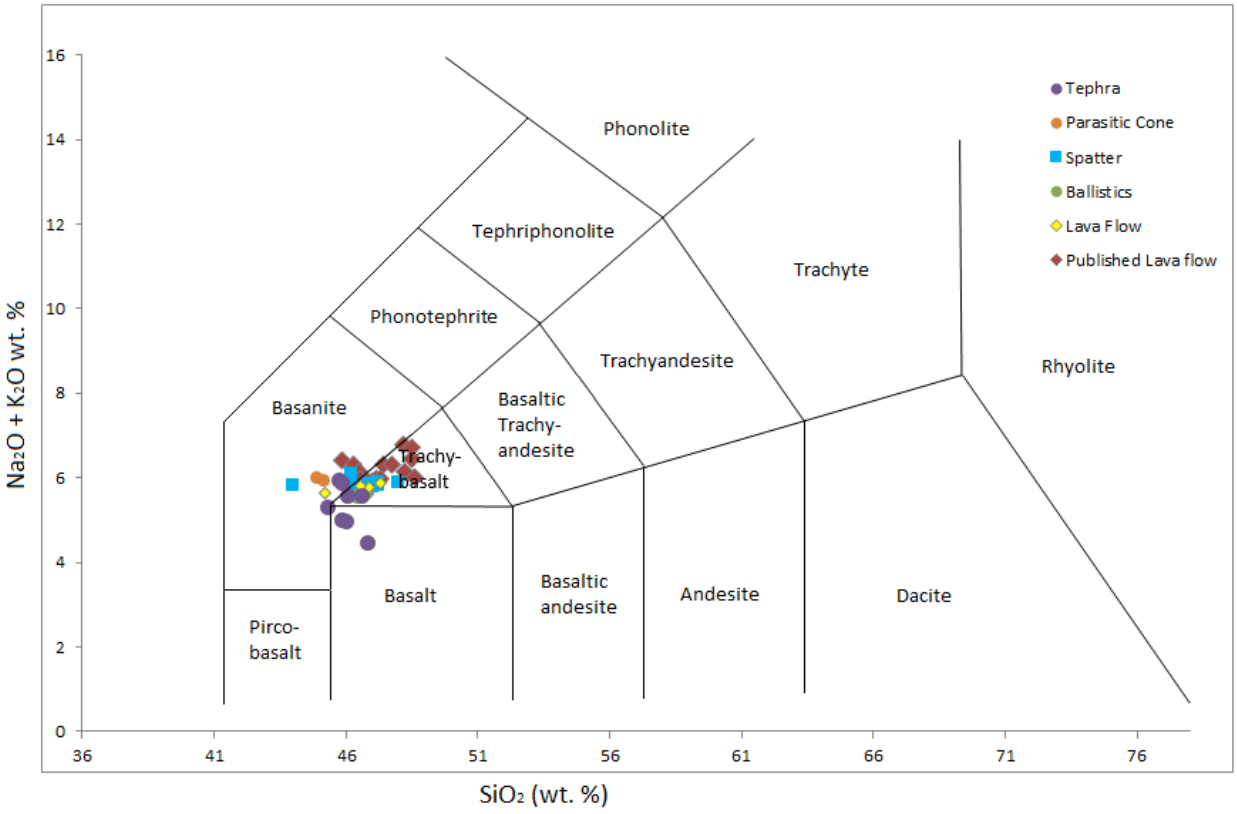

Figure 6.5.1 - Total Alkali Silica Diagram showing new Tseax data and published lava flow data

6.2 Eruptive style and tephra column parameters

The homogeneity of the grainsize distribution and Inman parameters throughout the tephra deposit indicate that the eruption of the main cone which produced the unoxidized tephra blanket was relatively steady in discharge rate, column height and direction throughout the course of the eruption. The distal deposits were not subject to significant sorting processes. These factors combined with the approximate mapped area of the tephra are consistent with a Hawaiian style eruption, probably including fire-fountaining and a weak plume.

The deposits of the parasitic cone could not be mapped away from the vent because of the great thickness of the main tephra deposit overlying them. Similarly, the tephra deposits of the outer spatter cone could not be mapped. However, the tephra deposits associated with these vents can be

inferred to be significantly smaller in area than those from the main cone as no distinct tephra layers were found either outside the limits of the main tephra deposits or underlying these deposits where their full thickness could be observed. The proximal deposits are dominated by oxidized material and contain significant spatter and large fluidal clasts. This indicates that the material forming these cones was erupted at high temperatures and cooled slowly. They were probably formed by fire-fountains of very limited height and therefore lacked significant tephra columns.

The isopach and ballistic velocity data for Tseax can be compared to observed Hawaiian eruptions to make inferences about volume, fire-fountain height, and eruption duration. Three well documented Hawaiian eruptions in Hawaii are the 1983-1986 eruption of Kilauea Iki, the 1959 eruption of Pu'u 'O'o and the 1969 eruption of Mauna Ulu. Kilauea Iki had the tallest fire fountain of these, reaching a maximum height of 579 m above the vent, with an average of 314 m (Houghton and Gonnermann 2008). Numerous isopach maps exist for the deposits of this eruption and show, on average, a deposit that stretches 3.2 km from the vent to the 1 cm isopach in the longest axis of the deposit (Klawonn 2013). The estimated tephra volume associated with the fire fountaining episodes was 1.5×10^8 m^3 and this was deposited over 13 days. Pu'u 'O'o had a fire fountain of maximum height 467 m and average height 256 m. The fire fountaining eruptive phase lasted for 47 days and produced 5.00×10^8 m^3 of tephra. Mauna Ulu produce a fire fountain of maximum 540 m and average 226 m, which lasted ten days and produced 6.50×10^7 m^3 of tephra. The average discharge rates during the fire fountain for Kilauea Iki, Pu'u 'O'o and Mauna Ulu respectively were 1.7×10^6 kgs^{-1}, 9.7×10^5 kgs^{-1} and 1.2×10^6 kgs^{-1} (Houghton and Gonnermann 2008).

The total volume for the main unoxidized tephra deposit of Tseax is estimated to be on the order of 10^6 m^3, one order of magnitude less than the smallest of these eruptions, Mauna Ulu. Consequently, the eruption of Tseax can be expected to have a lower discharge rate, duration or both than Mauna Ulu. At the same discharge rate the volume of tephra estimated at Tseax could be produced in one day. I therefore hypothesize an average fountain height of less than 230 m and lasting for a period of less than a week.

The height of the tephra column associated with the eruption of the main cone can be approximated using the methods of Carey and Sparks (1986) which correlate the maximum dispersal distance of clast sizes with column height. At the most distal sample locations, approximately 1.3 km from the vent, lapilli larger than 16 mm in diameter was rare, accounting for less than 1.4 % of the sampled material. The clast support envelopment for tephra of 16 mm diameter was thus inferred to

extend approximately 1.3 km in the downwind direction and out to the edge of the deposit, approximately 0.98 km, in the upwind direction. The minimum and maximum envelop widths were first compared to figures showing support envelops for eruptions unaffected by wind and carrying clasts of 2500 kg/m^3. This model produced overestimates of the column height of approximately 5 km for the minimum envelop and slightly less than 10 km for the maximum envelop. The maximum envelop was then compare to a model with windspeed 10 m/s, roughly twice what was used when modelling the Tseax eruption, and a low clast density of 500 kg/m^3. This model provided an underestimate of the column height at approximately 5 km. I therefore posit that the tephra column formed in the eruption of the main vent at Tseax Cone would have reached a height of slightly more than 5 km.

Different versions of the Nisga'a oral history of the eruption alternatively mention or do not mention a 'a big pillar of smoke' observed in the mountains shortly before the arrival of the lava flow in the villages (Barbeau 1935). A line of sight from the approximate locations of the two Nisga'a villages destroyed in the eruption shows that a 5 km column would have been easily visible from both villages although its source would have been unclear.

Using the approximated minimum 5 km column height the volume flux, and thus the eruptive duration can also be approximated. The equation

$$H = 1.67Q^{0.259}$$

can be used to estimate a volume flux for the explosive portion of the eruption. The volume previously estimated for the tephra deposits is divided by this flux to determine an approximate minimum eruption duration of 1 day for the main tephra column. This corresponds well with the estimate from comparison with Mauna Ulu and implies that the discharge rate could have been similar to Mauna Ulu's.

6.3 Eruptive History

The field and lab data collected on the pyroclastic deposits of Tseax cone allow for a new hypothesis for the eruptive history of Tseax Cone. It is proposed that the eruption began with fire fountaining, possible along a rift which very quickly localized to the sites of the parasitic and outer cones. Lack of observed overlap in the deposits means that which began or ended first cannot be inferred. The fire fountains associated with these vents would most likely have been only tens of meters high.

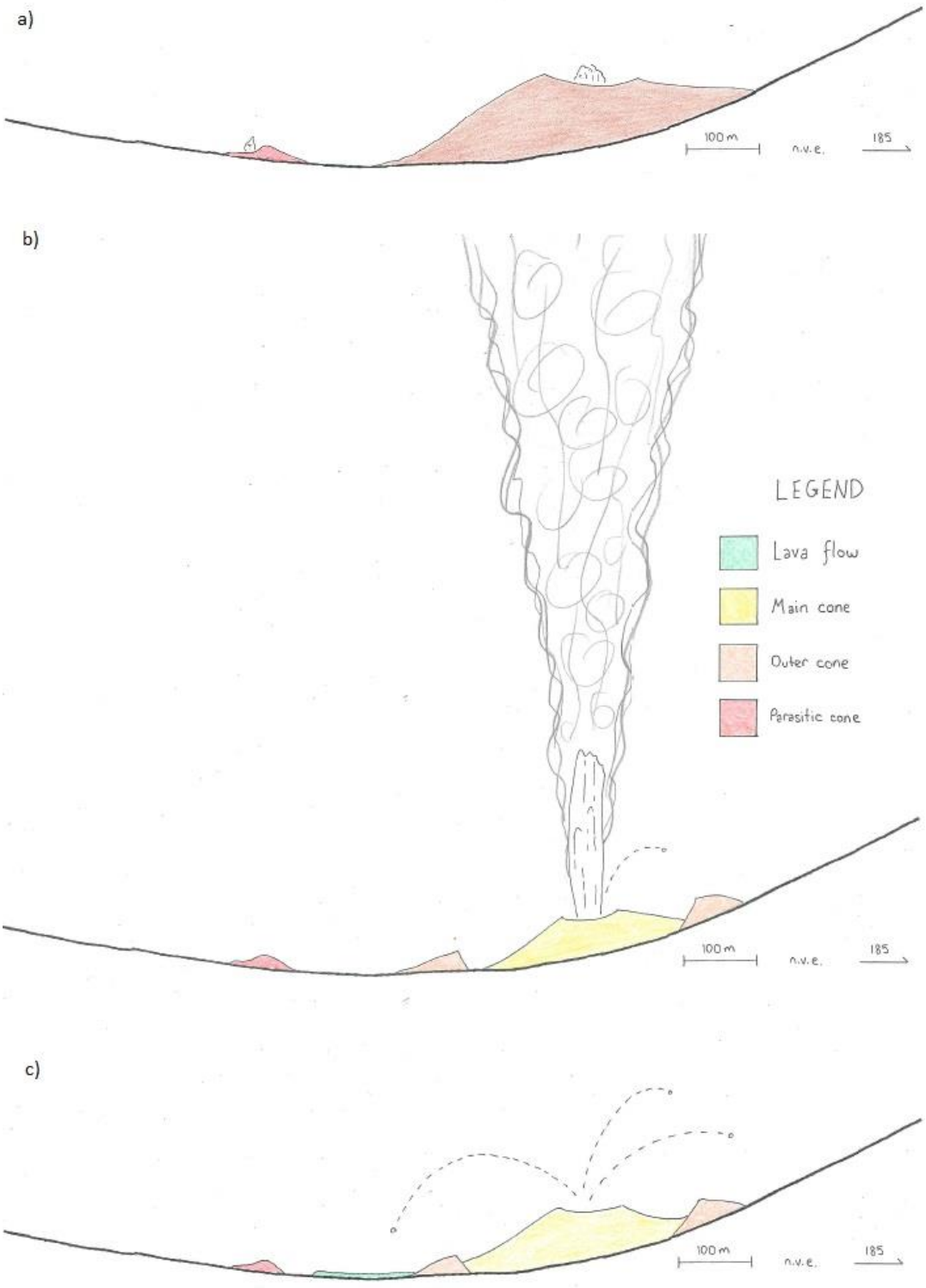

Figure 6.3.1 - Proposed eruptive phases. a) Low energy fire fountaining forms the outer and parasitic cones. b) Energetic fire fountaining and a sustained tephra column form the main cone and the tephra deposits. The outer cone is partially destroyed. c) Explosive activity is reduced to the ejection of ballistics and the effusive phase begins. The figures are approximately to scale.

Once eruption from both vents had terminated the eruption of the main cone began after a span of less than a year. This eruption was probably responsible for the partial destruction of the now highly dissected and incomplete outer cone. The presence of unoxidized spatter material from the main cone on the dissected rampart of the outer cone, indicates that the dissection of the outer cone occurred before or during the eruption of the main cone and is not the result of later weathering. Fire fountaining and a tephra column would have been produced from the main vent producing the main cone and tephra deposits and expelling some ballistics, for approximately one day. The final stage of the eruption was the lava flow which was accompanied by the ejection of a few remaining ballistics. The lava flow was not accompanied by fallout except perhaps in the initial stages.

Having produced a tephra deposit that was strongly skewed to the northeast, it is mostly likely that the eruption of the main cone occurred during the summer or early fall when winds from the southwest are most common in the region (WeatherSpark.com 2018). This is consistent with Nisga'a oral histories indicating that the eruption of the lava flow occurred during salmon spawning (Nisga'a Lisims Government 2017). Wind direction during the spatter cone and parasitic cone eruptions cannot yet be determined. It is possible that even if isopach maps could be developed for these vents any direction of deposit elongation would not be the result of overall wind direction but would be more strongly influenced by topography and more irregular ground-level wind patterns as genuine tephra columns likely did not develop (Parcheta et al 2012).

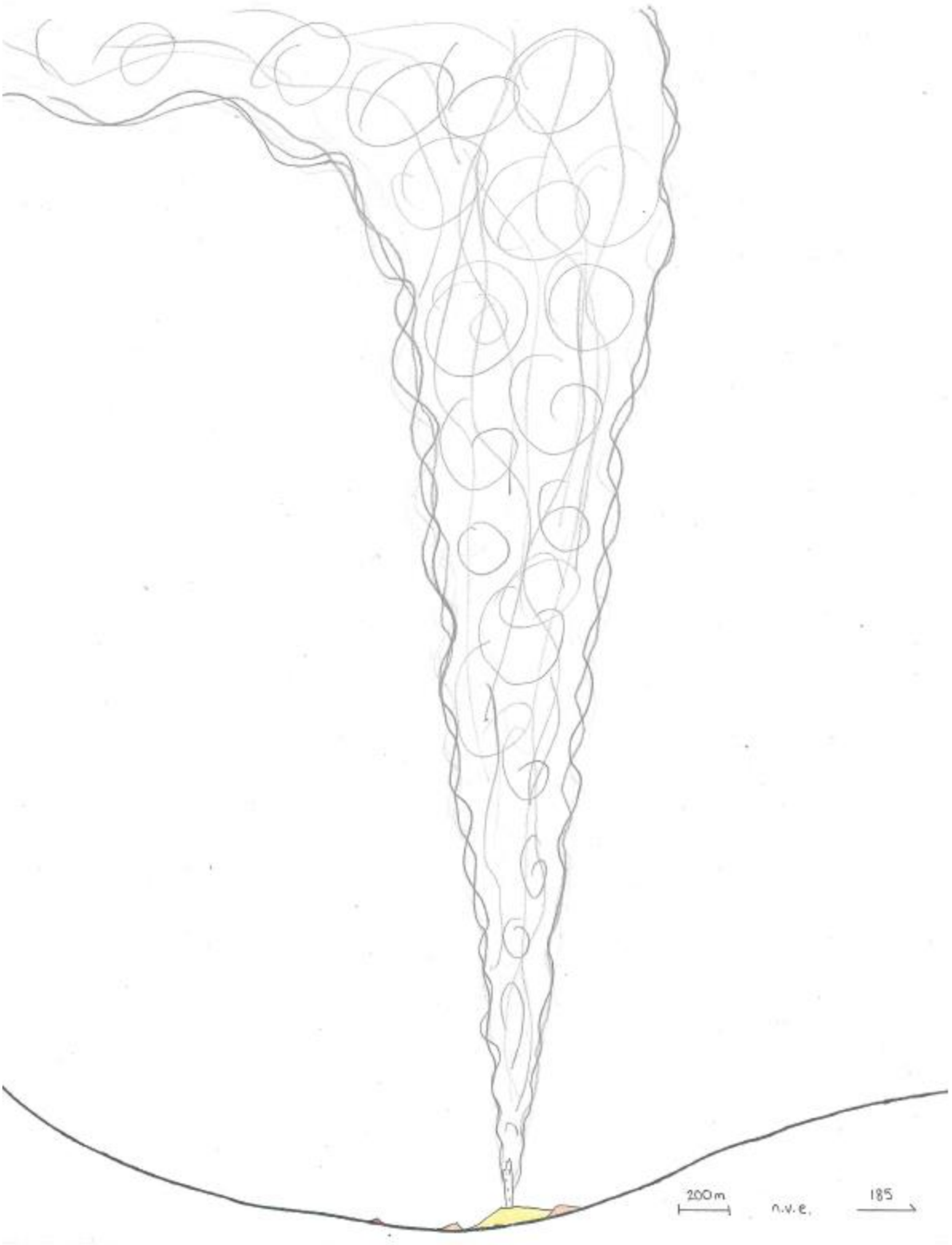

Figure 6.3.6 - The high energy eruptive phase featuring a fire fountain of approximately 200 m and a tephra column of just over 5 km erupting from the main vent.

CONCLUSION

The eruption of Tseax Cone is possibly the youngest and very probably the deadliest known volcanic eruption in Canadian history. This study aims to the provide a preliminary overview of the distribution and features of the pyroclastic products of Tseax Cone in order to develop new hypotheses for the explosive phase of the eruptive history of Tseax. The eruptive history of Tseax is newly constrained to a single period of eruptive activity including the formation of the parasitic cone and outer cone, follow by the main cone and tephra deposit, and finally the lava flow. The most energetic phase of the eruption, which produced the main cinder cone and the tephra deposit, consisted of energetic fire fountaining and an tephra column of slightly greater than 5 km height which was strongly skewed to the northeast.

REFERENCES

Barbeau, M., (1935). Volcanoes on the Nass. Canadian Geographical Journal 10(5): 215-225.

Bertin, D. (2017). 3-D ballistic transport of ellipsoidal volcanic projectiles considering horizontal wind field and variable shape-dependent drag coefficients. *Journal of Geophysical Research: Solid Earth*, *122*(2), 1126-1151.

Brown, A. S. (1969). Aiyansh lava flow, British Columbia. *Canadian Journal of Earth Sciences*, *6*(6), 1460-1468.

Carey, S., & Sparks, R. S. J. (1986). Quantitative models of the fallout and dispersal of tephra from volcanic eruption columns. *Bulletin of volcanology*, *48*(2-3), 109-125.

Crowe, C. T., Elger, D. F., Williams, B. C., & Roberson, J. A. (2009). Engineering fluid mechanics (9th ed.). Jefferson City: Wiley and Sons, Inc.

Edwards, B. R., & Russell, J. K. (1999). Northern Cordilleran volcanic province: A northern Basin and Range? *Geology*, *27*(3), 243-246.

Edwards, B. R., & Russell, J. K. (2000). Distribution, nature, and origin of Neogene–Quaternary magmatism in the northern Cordilleran volcanic province, Canada. *Geological Society of America Bulletin*, *112*(8), 1280-1295.

Environment and Climate Change Canada. (2017). *Climate data: homogenized wind speed data access.* Retrieved from https://www.canada.ca/en/environment-climate-change/services/climate-change/modelling-projections-analysis/adjusted-homogenized-canadian-data/wind-speed-access.html

Erdman, L. R. (1985). *Chemistry of neogene basalts of British Columbia and the adjacent pacific ocean floor: a test of tectonic discrimination diagrams* (Doctoral dissertation, University of British Columbia).

Hanson, G. (1923). Reconnaissance between Skeena River and Stewart, British Columbia. *Geol. Survey of Canada, Summary Report for*, 29-45.

Harder, M., & Russell, J. K. (2006). Thermal state of the upper mantle beneath the Northern Cordilleran Volcanic Province (NCVP), British Columbia, Canada. *Lithos*, *87*(1), 1-22.

Higgins, M. D. (2009). The Cascadia megathrust earthquake of 1700 may have rejuvenated an isolated basalt volcano in western Canada: Age and petrographic evidence. *Journal of Volcanology and Geothermal Research*, *179*(1-2), 149-156.

Houghton, B. F., & Gonnermann, H. M. (2008). Basaltic explosive volcanism: constraints from deposits and models. *Chemie der Erde-Geochemistry*, *68*(2), 117-140.

Klawonn, M. (2013). *Studies of pyroclastic fall transport and deposition* (Doctoral dissertation, [Honolulu]:[University of Hawaii at Manoa],[December 2013]).

Konstantinou, K. I. (2015). Maximum horizontal range of volcanic ballistic projectiles ejected during explosive eruptions at Santorini caldera. *Journal of Volcanology and Geothermal Research*, *301*, 107-115.

Larsen, J. F., Neal, C., Schaefer, J., Beget, J., & Nye, C. (2007). Late Pleistocene and Holocene Caldera-Forming Eruptions of Okmok Caldera, Aleutian Islands, Alaska. *Volcanism and subduction: The Kamchatka region*, 343-364.

Lowdon, J. A., Robertson, I. M., & Blake, W. (1971). Geological Survey of Canada radiocarbon dates XI. Radiocarbon, 13(2), 255-324.

Mastin, L. G. (2008). Eject! (Version 1.4) [Computer Software]. US Geological Survey. Available from https://pubs.usgs.gov/of/2001/0045/

Nicholls, J., Stout, M. Z., & Fiesinger, D. W. (1982). Petrologic variations in Quaternary volcanic rocks, British Columbia, and the nature of the underlying upper mantle. *Contributions to Mineralogy and Petrology*, *79*(2), 201-218

Nicholson, I. L. (2008). *Assessment of Volcanic Gas and Lava Flow Hazards Associated with the Historical Eruption of the Tseax Volcano, British Columbia* (Doctoral dissertation, University of Bristol).

Nisga'a Lisims Government. (2017). *Volcano.* Retrieved from http://www.nisgaanation.ca/volcano

Parcheta, C. E., Houghton, B. F., & Swanson, D. A. (2012). Hawaiian fissure fountains 1: decoding deposits—episode 1 of the 1969–1974 Mauna Ulu eruption. *Bulletin of Volcanology*, *74*(7), 1729-1743.

Sato, H., & Taniguchi, H. (1997). Relationship between crater size and ejecta volume of recent magmatic and phreato-magmatic eruptions: Implications for energy partitioning. *Geophysical Research Letters*, *24*(3), 205-208.

Stovall, W. K., Houghton, B. F., Hammer, J. E., Fagents, S. A., & Swanson, D. A. (2012). Vesiculation of high fountaining Hawaiian eruptions: episodes 15 and 16 of 1959 Kīlauea Iki. *Bulletin of volcanology*, *74*(2), 441-455.

Sun, S. S., & McDonough, W. S. (1989). Chemical and isotopic systematics of oceanic basalts: implications for mantle composition and processes. *Geological Society, London, Special Publications*, *42*(1), 313-345.

Taddeucci, J., Alatorre-Ibargüengoitia, M. A., Cruz-Vázquez, O., Del Bello, E., Scarlato, P., & Ricci, T. (2017). In-flight dynamics of Volcanic Ballistic Projectiles. *Reviews of Geophysics*.

Taddeucci, J., Scarlato, P., Capponi, A., Del Bello, E., Cimarelli, C., Palladino, D. M., & Kueppers, U. (2012). High-speed imaging of strombolian explosions: The ejection velocity of pyroclasts. *Geophysical Research Letters*, *39*(2).

The Weather Network. (2017). *Historical Weather: Terrace, BC*. Retrieved December 04, 2017, from https://www.theweathernetwork.com/weather/historical-weather/cabc0292

Van Der Heyden, P., Woodsworth, G. J., & Snyder, L. D. (2000). *Reconnaissance geological mapping in southwest Nass River map area, British Columbia*. Natural Resources Canada, Geological Survey of Canada.

Veness, C. Calculate distance, bearing and more between Latitude/Longitude points, from https://www.movable-type.co.uk/scripts/latlong.html

WeatherSpark.com. (2018) *Average Weather in Terrace Canada*. Retrieved March 12, 2018, from https://weatherspark.com/y/300/Average-Weather-in-Terrace-Canada-Year-Round

Wuorinen, V. (1978). Age of Aiyansh Volcano, British Columbia. *Canadian Journal of Earth Sciences*, *15*(6), 1037-1038.

LIST OF FIGURES

LIST OF TABLES

LIST OF APPENDICES

Appendix A: Major Element concentrations of tephra, bombs, spatter and lava from XRF analysis

Element Oxides (wt %)	RG-S6u	RG-S6L	RG-S5	RG-S16	RG-S25	RG-S22b	TS-S78
	Tephra						
SiO_2	46.81	45.82	45.3	46.58	46.04	46	45.70
TiO_2	3.61	3.62	3.47	3.67	3.66	3.56	3.39
Al_2O_3	14.34	14.36	14.14	14.6	14.36	14.51	14.45
Fe_2O_3	5.69	12.68	11.39	2.58	2.31	5.01	1.66
FeO	11.72	4.25	5.35	14.34	14.78	12.06	14.89
MnO	0.23	0.22	0.22	0.22	0.22	0.22	0.22
MgO	4.36	4.29	4.29	4.4	4.38	4.26	4.18
CaO	7.28	6.85	7.17	7.37	7.34	7.3	7.29
Na_2O	2.71	3.22	3.49	3.82	3.81	3.18	4.05
K_2O	1.74	1.76	1.8	1.76	1.75	1.77	1.89
P_2O_5	1.12	1.12	1.16	1.17	1.12	1.18	1.19
CO_2	0.14	0.07	0.16	0.54	0.33	0.42	
SO_3	0.21	0.21	0.16	0.21	0.22	0.15	
S	0.09	0.1	0.07	0.08	0.09	0.07	
Totals	99.03	98.75	98.69	100.2	99.27	98.95	
LOI	-1.04	0.11	0.48	-0.82	-0.98	-0.51	-0.85
FeO(T)	18.72	17.40	17.34	18.52	18.74	18.41	18.21

Element Oxides (wt %)	TS-S55	TS-S04	RG-B7	RG-B2	TS-S56	TS-S19
	Tephra		Bomb		Spatter	
SiO_2	45.80	46.79	46.4	46.74	47.30	46.85
TiO_2	3.40	3.56	3.64	3.56	3.51	3.59
Al_2O_3	14.65	14.70	14.46	14.62	14.40	14.57
Fe_2O_3	1.66	1.62	3.56	2.64	1.64	1.65
FeO	14.94	14.54	13.50	14.23	14.76	14.77
MnO	0.22	0.22	0.23	0.23	0.22	0.22
MgO	4.23	4.51	4.43	4.39	4.28	4.56
CaO	7.30	7.45	7.45	7.45	7.61	7.42
Na_2O	4.03	4.10	3.82	3.85	4.05	3.95
K_2O	1.86	1.84	1.76	1.81	1.81	1.83
P_2O_5	1.19	1.18	1.13	1.2	1.18	1.18
CO_2		0.12	0.07	0.07		0.14
SO_3		0.12	0.13	0.15		0.14
S			0.05	0.07		
Totals			99.69	99.79		
LOI	-0.74	-1.03	-1.11	-1.34	-0.76	-1.00
FeO(T)	18.26	17.78	18.56	18.45	18.04	18.06

Element Oxides (wt %)	TS-S20	TS-S06	TS-S62	TS-S63	TS-S02	TS-S47	TS-S48
	Spatter				Lava flow		
SiO_2	46.54	45.20	46.80	48.00	46.20	46.30	47.20
TiO_2	3.68	3.33	3.53	3.58	3.48	3.36	3.53
Al_2O_3	14.54	13.70	14.25	14.65	14.30	14.60	14.30
Fe_2O_3	1.64	2.01	1.63	1.65	1.62	1.60	1.64
FeO	14.69	18.08	14.62	14.85	14.53	14.40	14.76
MnO	0.22	0.26	0.22	0.22	0.22	0.22	0.22
MgO	4.65	4.11	4.44	4.39	4.35	4.31	4.30
CaO	7.44	7.05	7.48	7.78	7.42	7.37	7.62
Na_2O	4.02	3.90	3.97	4.08	4.06	3.99	4.07
K_2O	1.78	1.73	1.82	1.79	1.87	1.78	1.82
P_2O_5	1.12	1.07	1.15	1.15	1.19	1.15	1.19
CO_2	0.06						
SO_3	0.06						
S							
Totals							
LOI	-0.37	-2.40	-1.16	-1.14	-1.14	-0.84	-1.11
FeO(T)	17.97	22.10	17.88	18.15	17.77	17.60	18.04

Element Oxides (wt %)	TS-S50	TS-S52	TS-S60	TS-S51	TS-S26	TS-S33	TS-S57
	Lava Flow						
SiO_2	47.20	46.85	46.20	46.60	47.00	46.70	46.86
TiO_2	3.51	3.67	3.39	3.51	3.47	3.43	3.58
Al_2O_3	14.30	14.64	14.40	14.15	14.25	14.20	14.68
Fe_2O_3	1.64	1.64	1.81	1.63	1.62	1.61	1.63
FeO	14.71	14.74	16.24	14.67	14.53	14.44	14.63
MnO	0.22	0.22	0.24	0.22	0.22	0.22	0.22
MgO	4.33	4.64	4.22	4.36	4.24	4.21	4.51
CaO	7.59	7.51	7.37	7.54	7.57	7.49	7.45
Na_2O	4.01	4.03	4.16	3.94	3.98	3.95	3.90
K_2O	1.79	1.81	1.91	1.77	1.80	1.78	1.80
P_2O_5	1.16	1.16	1.20	1.15	1.17	1.18	1.18
CO_2		0.14					0.09
SO_3		0.14					0.09
S							
Totals							
LOI	-1.13	-1.38	-1.18	-0.97	-0.81	-0.77	-0.93
FeO(T)	17.99	18.02	19.86	17.93	17.77	17.66	17.89

Element Oxides (wt %)	TS-S71	TS-S68	TS-S40B	TS-S40A	RG-S22a	TS-S44
	Lava Flow		Parasitic Cone			Lithic
SiO_2	46.20	44.00	44.90	45.20	46.1	50.84
TiO_2	3.31	3.25	3.45	3.46	3.63	2.97
Al_2O_3	14.05	13.75	14.20	14.25	14.45	14.58
Fe_2O_3	1.88	2.21	1.67	1.67	14.24	1.41
FeO	16.92	19.84	15.03	14.98	2.85	12.63
MnO	0.24	0.28	0.22	0.22	0.22	0.19
MgO	4.19	4.07	4.21	4.24	4.38	4.43
CaO	7.22	7.03	6.59	6.67	6.88	5.83
Na_2O	4.07	3.98	4.12	4.05	3.76	3.82
K_2O	1.85	1.81	1.87	1.86	1.76	1.71
P_2O_5	1.17	1.14	1.12	1.12	1.14	0.89
CO_2					0.07	0.08
SO_3					0.21	0.08
S					0.09	
Totals					99.86	
LOI	-1.54	-2.62	0.66	0.74	-0.02	0.21
FeO(T)	20.68	24.26	18.37	18.32	17.41	15.45

Appendix B: Trace Element concentrations of tephra, bombs, spatter and lava from ICP-MS analysis

Trace Elements (ppm)	RG-S25	TS-S78	TS-S55	TS-S04	RG-B2
	Tephra			Bomb	
Cs	0.29	0.22	0.27	0.22	0.22
Rb	24.2	23.7	24.3	22.6	24.4
Ba	897	887	925	909	950
W	<1	1	1	1	<1
Th	2.64	2.64	2.8	2.51	2.63
U	0.86	0.86	0.89	0.82	0.84
Nb	36.7	35.2	36.8	35.7	37.1
Ta	2.3	2.1	2.2	2	2.3
La	30.3	30.3	31.9	29.3	31
Ce	65.1	66.4	69.2	62.3	67.2
Pr	8.62	8.5	9.13	8.06	8.9
Sr	468	480	505	466	471
Nd	38	37	39.8	35.9	38.5
Sm	8.91	8.71	9.53	9.09	9.22
Zr	226	195	206	219	226
Hf	5.2	4.9	5.1	4.9	4.9
Eu	3.58	3.81	3.78	3.61	3.76
Sn	2	2	2	2	5
Gd	9.48	9.19	9.63	9.09	9.84
Tb	1.22	1.33	1.35	1.35	1.28
Dy	7.48	7.25	7.84	7.39	7.38
Y	34.5	35.7	38.1	33.8	35.5
Ho	1.25	1.39	1.47	1.37	1.39
Er	3.3	3.02	3.47	3.39	3.64
Tm	0.46	0.46	0.49	0.43	0.45
Yb	2.69	2.64	2.7	2.68	2.64
Lu	0.36	0.41	0.42	0.4	0.36
Cr	20	20	20	10	20
Ga	26.1	24.1	25.5	24.9	26.4
V	185	173	183	164	171

Trace Elements (ppm)	TS-S56	TS-S19	TS-S20	TS-S06	TS-S62	TS-S63	TS-S02
	Spatter				Lava flow		
Cs	0.2	0.25	0.21	0.21	0.2	0.22	0.24
Rb	22.5	22.4	21.9	20.5	21.5	21.4	22.5
Ba	909	878	833	802	835	851	923
W	1	1	1	1	6	2	1
Th	2.44	2.41	2.44	2.63	2.47	2.34	2.58
U	0.78	0.74	0.76	0.82	0.73	0.7	0.79
Nb	36.8	34.6	34	33.8	35.8	35.5	37.6
Ta	2.1	2	1.9	2.1	2	1.9	2.1
La	29.1	28.4	27.5	28.5	27.8	27.5	29.3
Ce	62.5	60.9	58.3	61	59.4	59.4	63.5
Pr	8.21	7.93	7.53	7.91	7.81	7.83	8.31
Sr	465	447	442	463	441	457	463
Nd	35.7	34.2	33.5	35.4	34.1	34	36.6
Sm	9	8.84	8.3	8.24	8	8.26	8.99
Zr	211	217	208	186	201	203	214
Hf	5.3	4.8	4.7	4.7	5	4.8	5.2
Eu	3.55	3.57	3.28	3.65	3.37	3.36	3.52
Sn	2	2	2	2	2	2	2
Gd	9.37	8.98	8.79	8.36	8.69	8.53	9.36
Tb	1.3	1.3	1.21	1.23	1.21	1.22	1.31
Dy	7.43	6.95	6.9	6.96	6.79	6.96	7.28
Y	33.8	33.2	32.5	33.5	32.1	31.9	33.9
Ho	1.35	1.37	1.27	1.31	1.26	1.3	1.34
Er	3.41	3.19	3.08	3.09	3.44	3.27	3.45
Tm	0.46	0.44	0.42	0.42	0.43	0.42	0.43
Yb	2.54	2.62	2.51	2.46	2.45	2.52	2.53
Lu	0.39	0.38	0.37	0.4	0.36	0.35	0.37
Cr	10	10	10	20	10	10	10
Ga	24.9	24.4	23.8	23.5	24.2	24.1	25.4
V	161	170	171	179	163	164	163

Trace Elements (ppm)	TS-S47	TS-S48	TS-S50	TS-S52	TS-S60	TS-S51	TS-S26	TS-S33
	Lava Flow							
Cs	0.21	0.23	0.21	0.21	0.22	0.26	0.18	0.21
Rb	21.4	22.5	21.7	22.4	24.1	22.5	22.1	21.4
Ba	869	897	867	844	921	877	896	894
W	1	7	2	1	1	1	3	1
Th	2.3	2.47	2.41	2.48	2.82	2.52	2.35	2.39
U	0.73	0.73	0.7	0.73	0.86	0.75	0.78	0.76
Nb	35.5	36.7	35.6	34.8	36.8	36.5	36.3	35.9
Ta	2	2	2	2	2.2	2	2	1.9
La	27.4	28.4	27.5	28.3	31.5	28.1	28.5	28.2
Ce	59.4	61.3	59.5	60	68.1	60.7	61.2	60.3
Pr	7.82	8.02	7.85	7.66	9.02	7.92	7.86	7.86
Sr	442	454	451	449	489	461	454	455
Nd	34.3	35.4	34	33.2	38.7	34.7	35.4	34.4
Sm	8.5	8.73	8.83	8.59	9.47	8.59	8.53	8.57
Zr	200	208	201	215	204	210	206	206
Hf	5	5.2	4.8	4.9	5.1	5.2	5	5.1
Eu	3.4	3.39	3.35	3.49	4.21	3.46	3.63	3.5
Sn	2	2	2	2	2	2	2	2
Gd	8.86	8.9	8.83	8.77	9.44	8.93	8.9	8.97
Tb	1.23	1.26	1.25	1.32	1.41	1.25	1.25	1.27
Dy	6.89	7.07	6.67	7.04	7.78	7.12	6.94	7.08
Y	32.2	33.2	32.4	32.8	37.2	33.5	33	32.9
Ho	1.27	1.3	1.32	1.35	1.46	1.32	1.3	1.33
Er	3.37	3.4	3.24	3.2	3.47	3.31	3.41	3.29
Tm	0.44	0.43	0.41	0.43	0.47	0.43	0.44	0.41
Yb	2.51	2.46	2.45	2.65	2.71	2.6	2.64	2.5
Lu	0.36	0.39	0.37	0.39	0.4	0.39	0.39	0.37
Cr	10	10	10	10	20	10	10	10
Ga	23.7	24.3	24.1	24.2	25.2	24.5	24.5	24.5
V	152	161	162	171	177	168	156	157

Trace Elements (ppm)	TS-S57	TS-S71	TS-S68	TS-S40B	TS-S40A	TS-S44	RG-S22a
	Lava Flow			Parasitic Cone			
Cs	0.21	0.23	0.23	0.34	0.34	0.89	0.91
Rb	23	23.1	23.3	24.9	25.7	27.7	26.6
Ba	935	840	860	852	881	816	897
W	1	1	1	1	1	1	<1
Th	2.54	2.68	2.64	2.77	2.81	2.7	2.6
U	0.82	0.79	0.82	0.89	0.92	0.95	0.84
Nb	36.7	34.4	35.1	35.6	37.4	27.9	36.5
Ta	2.1	2	2.2	2	2.2	1.6	2.2
La	30	29.2	30	30	31.1	24.7	30.1
Ce	63.9	63.3	65.5	64.7	67.5	52.3	65.8
Pr	8.27	8.3	8.69	8.51	8.86	6.8	8.83
Sr	473	461	477	455	463	391	442
Nd	36.5	35.5	36.8	36.5	38	29.7	38.5
Sm	9.29	8.67	9.07	9.36	9.24	7.33	9.01
Zr	223	189	196	196	203	188	223
Hf	4.9	4.7	4.8	4.8	4.9	4.4	5.1
Eu	3.87	3.69	3.8	3.83	3.79	2.92	3.59
Sn	2	2	2	8	8	7	9
Gd	9.53	8.91	8.95	9.1	9.16	7.36	9.52
Tb	1.32	1.31	1.3	1.3	1.34	1.12	1.24
Dy	7.41	7.06	7.54	7.62	8.02	6.06	7.19
Y	34.8	34.3	35.9	35.8	37	29.3	34.7
Ho	1.41	1.32	1.42	1.38	1.4	1.15	1.31
Er	3.36	3.08	3.4	3.52	3.55	2.7	3.49
Tm	0.48	0.43	0.45	0.45	0.45	0.38	0.44
Yb	2.78	2.83	2.66	2.79	2.78	2.36	2.58
Lu	0.39	0.38	0.42	0.4	0.42	0.39	0.36
Cr	10	30	20	10	20	60	10
Ga	25.3	23.5	24.7	24.6	25	22.7	25.9
V	168	170	177	184	191	165	179

Appendix C: Lower Limit of Reporting for Trace Element Analysis

Trace Element	LOR (ppm)
Ba	0.5
Ce	0.5
Cr	10
Cs	0.01
Dy	0.05
Er	0.03
Eu	0.03
Ga	0.1
Gd	0.05
Hf	0.2
Ho	0.01
La	0.5
Lu	0.01
Nb	0.2
Nd	0.1
Pr	0.01
Rb	0.2
Sm	0.03
Sn	1
Sr	0.1
Ta	0.1
Tb	0.01
Th	0.05
Tm	0.01
U	0.05
V	5
W	1
Y	0.5
Yb	0.03
Zr	2

Appendix D: Error in ALS Geochemical replicates

Major Elements	1σ (wt.%)
SiO2	0.15
TiO2	0.02
Al2O3	0.06
FeO(T)	0.03
MnO	0.01
MgO	0.07
CaO	0.15
Na2O	0.03
K2O	0.02
P2O5	0.01

Trace Elements	1σ (ppm)
La	1.6380
Ce	2.8553
Pr	0.3613
Nd	1.7341
Sm	0.2277
Eu	0.1240
Gd	0.4525
Tb	0.0545
Dy	0.2867
Ho	0.0730
Er	0.2009
Tm	0.0286
Yb	0.2032
Lu	0.0200
Ba	30.3282
Th	0.1199
Nb	1.8534
Y	2.0092
Hf	0.2608
Ta	0.1643
U	0.0464
Rb	0.8198
Cs	0.0158
Sr	42.3143
Zr	13.2778
Cr	13.0384
V	25.5578
Ga	1.2570

Appendix E: Major Element concentrations of Tseax lava flow from previous studies

Element Oxide (wt %)	Sutherland Brown (1969)	Hanson (1924)	Erdman 1985		Nicholls et al. 1982
	68AB70				Nr5-c
SiO_2	45.80	46.24	47.38	48.13	46.53
TiO_2	3.79	3.00	3.35	3.26	3.72
Al_2O_3	14.67	15.79	14.54	14.73	14.40
Fe_2O_3	2.12	2.86	0.00	0.00	2.27
FeO	13.64	11.81	13.99	13.32	12.76
MnO	0.22	0.15	0.22	0.21	0.29
MgO	2.30	4.43	4.24	3.58	4.52
CaO	9.81	7.94	7.58	7.55	7.53
Na_2O	3.83	2.40	4.71	5.09	4.12
K_2O	2.60	3.90	1.60	1.70	1.87
P_2O_5	0.87	1.00	0.83	0.94	1.15
CO_2	0.01				
SO_3		0.09			
SO_2					
S		0.04			
Cl					
H_20-	0.06				0.07
H_20+	0.11	0.10			0.16
FeO(T)	16.00	14.99	13.99	13.32	15.28

Element Oxide (wt %)	Nicholls (p.c. 2016)							
	NR4	NR3B	NR5	NR2B	NR6	NR11	NR12	NR74-1
SiO_2	46.40	46.49	46.53	46.97	47.12	47.15	47.15	46.80
TiO_2	3.68	3.66	3.72	3.60	3.66	3.55	3.55	3.53
Al_2O_3	14.41	14.30	14.40	14.43	14.56	14.80	14.70	14.70
Fe_2O_3	2.76	2.20	2.27	2.57	2.50	0.00	0.00	0.00
FeO	12.28	12.63	12.76	12.47	12.32	14.45	14.50	14.40
MnO	0.23	0.35	0.29	0.22	0.22	0.22	0.22	0.22
MgO	4.54	4.50	4.52	4.78	4.52	4.43	4.37	4.37
CaO	7.52	7.58	7.53	7.29	7.56	7.64	7.62	7.55
Na_2O	4.45	4.24	4.12	4.08	4.14	4.07	4.07	4.08
K_2O	1.66	1.92	1.87	1.82	1.82	1.83	1.84	1.84
P_2O_5	1.17	1.08	1.15	1.16	1.15	1.26	1.28	1.28
CO_2								
SO_3								
SO_2								
S								
Cl								
H_20-	0.08	0.07	0.07	0.03	0.06	0.00	0.00	0.00
H_20+	0.18	0.23	0.16	0.20	0.12	0.50	0.50	0.50
FeO(T)	15.35	15.07	15.28	15.33	15.10	14.45	14.50	14.40

Element Oxide (wt %)	Nicholson 2008 (Groundmass glass)					
	NR74-2	060304a	06wv55a	060304b	06wv50c	06wv50d
SiO_2	47.30	47.71	48.20	48.44	48.46	48.58
TiO_2	3.51	3.45	3.51	3.42	3.37	3.39
Al_2O_3	14.80	14.89	14.71	14.78	14.82	14.81
Fe_2O_3	0.00	0.00	0.00	0.00	0.00	0.00
FeO	14.30	13.11	13.25	14.09	13.75	13.65
MnO	0.22	0.26	0.21	0.20	0.21	0.22
MgO	4.24	3.71	3.78	3.69	3.83	3.75
CaO	7.63	8.05	7.96	7.85	7.93	8.23
Na_2O	4.09	4.40	3.97	4.39	4.65	4.33
K_2O	1.88	1.91	2.16	2.07	2.07	1.69
P_2O_5	1.31	1.33	1.34	1.16	1.29	1.20
CO_2						
SO_3						
SO_2		0.16	0.14	0.14	0.15	0.16
S						
Cl		0.03	0.05	0.04	0.04	0.04
H_20-	0.00					
H_20+	0.50					
FeO(T)	14.30	13.11	13.25	14.09	13.75	13.65